Shati, a novel molecule containing a conserved sequence of the *N*-acetyltransferase superfamily, is expressed in the NAc in mice treated with METH (Niwa et al., 2007). Recently, Shati was shown to generate *N*-acetylaspartate (NAA) from aspartate as an *N*-acetyltransferase 8-like protein (Nat8l) (Ariyannur et al., 2010). Shati/Nat8l mRNA expression was induced by treatment with METH in the NAc and dS (Niwa et al., 2007). Knock down of Shati/Nat8l expression by intraventricular administration of antisense oligonucleotide in mice potentiates METH-induced behavioral alterations and increases extracellular DA levels in the NAc (Niwa et al., 2007). Furthermore, NAA undergoes conversion to *N*-acetylaspartylglutamate (NAAG), an endogenous metabotropic glutamate receptor type 3 (mGluR3) agonist, via NAAG synthase in neurons (Becker et al., 2010). Thus, a functional role of Shati/Nat8l should be regulated by NAA and NAAG activity. However, the efficacy of Shati/Nat8l expression in specific brain regions on METH-induced responses has not been clarified. Moreover, the mechanism of Shati/Nat8l regulation of METH-induced DA elevation is unknown.

In this study, Shati/Nat8l was overexpressed in the NAc or dS to clarify its mechanism in METH addiction and its regional specificity of function. Overexpression of Shati/Nat8l in the NAc, but not in the dS, of mice attenuated METH-induced hyperlocomotion, locomotor sensitization, CPP and elevation of extracellular DA levels. Treatment with LY341495, an antagonist for group II mGluRs (mGluR2/3), inhibited those suppressive efficacies on behavioral and neurochemical alterations by Shati/Nat8l overexpression in the NAc. In addition, the tissue contents of NAA and NAAG were increased in the AAV vector-injected NAc accompanied with a decreased extracellular DA level. These results suggest that activation of gruop II mGluRs in the NAc is important for the suppressive function of Shati/Nat8l in METH-induced addiction.

Materials and methods

Animals

Male C57BL/6J mice (Nihon SLC, Inc., Japan) were 8 wk old and weighed 22–27 g at the beginning of the experiments. Animals were housed in a room with 12 h light/dark cycle (lights on 08:00 hours). Food and water were available *ad libitum*. All experiments followed the National Institute of Health Guidelines for the Care and Use of Laboratory Animals and were approved by the committee for Animal Experiments of the University of Toyama.

Drugs

METH hydrochloride and pentobarbital were obtained from Dainippon Sumitomo Pharmaceutical Co. (Japan) and were dissolved in saline. NAAG, 2-(phosphonomethyl) pentanedioic acid (2-PMPA), and LY341495 were purchased from Tocris Bioscience (USA). NAAG and 2-PMPA were dissolved in saline. LY341495 was dissolved in 0.125 M phosphate buffer (pH 8.00). NAA was purchased from Sigma-Aldrich (USA).

Production of AAV vector

The production of AAV vector was described previously (Krzyzosiak et al., 2010). Briefly, the AAV vector plasmids contained an expression cassette, consisting of a human cytomegalovirus immediate–early promoter (CMV promoter), followed by cDNA encoding either Shati/Nat8l (Shati: GenBank accession number NM_001001985) or EGFP, and a simian virus 40 polyadenylation signal sequence (SV40 poly (A)), between the inverted terminal repeats of the AAV3 genome. The recombinant AAV vectors were produced by transient transfection of HEK293 cells using the vector plasmid; an AAV2 rep and AAV1 vp expression plasmid, and the adenoviral helper plasmid, pHelper (Agilent Technologies). The recombinant viruses were purified by isolation from two sequential continuous CsCl gradients, and the viral titers were determined by qRT-PCR.

Microinjection of AAV vector

Under pentobarbital (50 mg/kg, i.p.) anesthesia, mice were fixed in a stereotactic frame (SR-5M, Narishige, Japan). AAV-Shati vector (10^{10} to 10^{12} unit/0.7 μl/side) suspension was injected bilaterally into the NAc (1.4 mm anterior and 0.6 mm lateral from bregma, 4.2 mm below skull surface) or dS (0.5 mm anterior and 2.0 mm lateral from bregma, 3.5 mm below skull surface) according to the atlas (Paxions and Franklin, 2008). Injection volume was set as in previous studies (Krzyzosiak et al., 2010). The injection was carried out at 0.05 μl/min, and the needle was left at rest in the brain for 10 min after the end of the injection. Mice were used for the experiments 3 wk later.

Quantitative RT-PCR

Whole brains were removed and divided into 1 mm thick sections using mouse brain matrix. Tissue corresponding to the NAc was collected with a 1 mm punch from the section. Similarly, dS tissue was collected using a 1 mm punch from subsequent sections. The accurate location of these brain structures was based on visual inspection of each section using a stereomicroscope and comparison with the stereotaxic atlas of mouse brain (Franklin and Paxinos, 2008). Tissue samples were placed on dry ice and kept at −80 °C until use. Total RNA extraction was carried out using the RNeasy Plus Mini Kit protocol (QIAGEN, Japan). Total RNA from each tissue sample was transcribed into cDNA using the Prime Script RT reagent kit (Takara, Japan) according to the manufacturer's

recommendation. Briefly, the reaction was carried out at 37 °C for 20 min in a total volume of 10 μl and was inactivated at 85 °C for 5 s. Twenty-times diluted cDNA was used as a template, and quantitative real-time PCR was run in a Thermal Cycler Dice Real Time System (Takara) using Power SYBR Green PCR Master Mix (Applied Biosystems, USA) with cDNA and genespecific primers (1 μM) following the manufacturer's instructions. All of the reactions were performed in duplicate with the following cycling protocol: 10 min of heat activation of the enzyme at 95 °C, 45 cycles of denaturation at 95 °C for 5 s, annealing at 60 °C for 30 s, and extension at 72 °C for 20 s. The Shati/Nat8l primers used for real-time PCR were as follows: 5'-GTGATTCTGGCCTACCTGGA-3' (forward bp 457–477) and 5'-CCACTGTGTTGTCCTCCTCA-3' (reverse bp 616–636). *36B4* transcript was used as the internal control. *36B4* transcript amount was quantified using forward primer 5'-ACCCTGAAGTGCTCGACATC-3' and reverse primer 5'-AGGAAGGCCTTGACCTTTTC-3'.

In situ *hybridization*

Adult mice were anesthetized with a lethal dose of sodium pentobarbital (50 mg/kg) and perfused through the left ventricle with 50 ml of phosphate buffered saline (PBS) to flush the blood vessels quickly, followed by 50 ml of cold 4% paraformaldehyde (PFA) in PBS. The brains were removed from the skull, postfixed in 4% PFA at 4 °C overnight, followed by cryoprotection in 30% sucrose in PBS overnight at 4 °C. Serial coronal sections of the whole brain were cut at 20 μm thickness on a cryostat. We selected this thickness to check expression of AAV vector-induced genes in the injection brain site (Leica CM 3050, Japan).

To generate antisense riboprobes, mouse cDNA sequences for Shati/Nat8l (bp 1133–1557) were amplified by PCR and cloned into the pGEM-T Easy vector (Promega, USA). Digoxigenin (DIG)-labeled antisense and sense cRNA probes were synthesized from linearized plasmids using T7 and SP6 RNA polymerase (Roche, Germany), according to the instructions of the manufacturer. Brain sections from mice were hybridized to antisense and sense cRNA probes as described previously with modification (Nitta et al., 1999). Sections were covered with the hybridization buffer (10% dextran sulfate, 5×standard saline citrate (SSC), 20 mM Tris-HCl pH 8.00, 300 mM NaCl, 50% formamide, 1×Denhardt's solution and 500 ng/ml yeast tRNA) containing 25 ng/ml salmon sperm DNA at 65 °C for 1 h, and then incubated with hybridization buffer containing a DIG-labeled cRNA probe at 65 °C for 16 h. Post-hybridization washes were performed stepwise with 4×SSC at 65 °C for 20 min, 50% formamide in 2×SSC at 65 °C for 30 min, TNE buffer (500 mM NaCl, 10 mM Tris-HCl buffer pH 7.50, 1 mM EDTA) at 37 °C for 10 min, 4 ng/ml RNase A in TNE buffer at 37 °C for 30 min, TNE buffer at 37 °C for 10 min, 2×SSC at 65 °C for 30 min, 0.2×SSC at 65 °C for 30 min, buffer A (150 mM NaCl, 100 mM Tris-HCl pH 7.50) at room temperature for 10 min, and buffer B (1.5% blocking reagent in buffer C [100 mM NaCl, 100 mM Tris-HCl pH 9.50, 50 mM $MgCl_2$]) for blocking at room temperature for 1 h. Subsequently, sections were washed with buffer B at room temperature, and then incubated with 0.75 U/ml anti-DIG-AP Fab fragments in buffer B containing 0.2% Tween-20 at 4 °C for 16 h. After washing with buffer B containing 0.2% Tween-20 at room temperature for 15 min, sections were treated with buffer C, and then with buffer C containing NBT/BCIP Stock Solution (Roche) for different periods to obtain images most appropriate for subsequent development. After washing with buffer C at room temperature for 5 min, the development was stopped by incubation in 1×TE (10 mM Tris-HCl pH 7.5, 1 mM EDTA pH 8.00). The histochemical staining signal was observed by an AxioObserver Z1 (Carl Zeiss, Germany).

Immunostaining

Sections were fixed with 4% PFA for 20 min, and incubated with 0.25% Triton X-100 for 15 min. Sections were treated with 10 mM citrate buffer (pH 6.00) for antigen retrieval at 95 °C for 10 min, washed with Tris buffered saline with Tween-20 (TBS-T), and then blocked in 10% goat serum for 1 h. Sections were incubated with rabbit antibody against GFP (1:1000, Abcam, USA) at 4 °C overnight, washed with TBS-T, and then incubated with CF™ 594 goat anti-rabbit IgG (H+L) (Biotium, USA) at room temperature for 2 h. After being washed and mounted, sections were observed.

Measurement of locomotor activity and sensitization

Mice were placed individually in a transparent acrylic cage with a black frosting Plexiglas floor (45×25×40 cm), and locomotor activity was measured every 5 min for 60 min using digital counters with infrared sensors (Scanet MV-40; MELQEST, Japan). METH (1 mg/kg s.c.) or saline was administered immediately before the measurement of locomotor activity. After repeated METH treatment for 7 d and following METH withdraw for 5 d, the re-challenge lower dose of METH (0.3 mg/kg s.c.) for locomotor sensitization was administered immediately before the measurement of locomotor activity on Day 13.

CPP test

The place conditioning test was performed according to the method of Miyamoto et al. (2004) and Furukawa-Hibi et al. (2010). Briefly, the apparatus consisted of two compartments: transparent and black Plexiglass boxes (both 15×15×15 cm) The floors of the transparent and

black boxes were covered with white and black frosted Plexiglass, respectively. Each box could be divided by a sliding door (10×15 cm high). In the pre-conditioning, the sliding door was opened and the mouse was allowed to move freely between both boxes for 15 min once a day for 3 d. On day 3, the time that the mouse spent in the transparent and black boxes was measured using the LD mode of a Scanet MV-40 (MELQEST). The box in which the mouse spent the most time was referred to as the 'preferred side', and the other box, the 'non-preferred side'. The conditioning was performed on six successive days. The mouse was given the drug or vehicle immediately before the conditioning in the apparatus with the sliding door closed. On days 4, 6 and 8, the mouse was given METH (1 mg/kg s.c.) or saline and placed in its non-preferred side for 20 min. On days 5, 7 and 9, the mouse was given saline and placed in its preferred side (opposite to the METH-conditioning side) for 20 min. On day 10, the post-conditioning was performed without drug treatment. In the post-conditioning, the sliding door was opened, and the time that the mouse spent in the transparent and black boxes during 15 min was measured as on day 3. Place conditioning behavior was expressed by Post – Pre, which was calculated as (post value) – (pre value), where post and pre values were the difference in time spent in the METH-conditioning and the saline-conditioning sides in post-conditioning and pre-conditioning, respectively.

In vivo *microdialysis*

We performed *in vivo* microdialysis as described previously (Niwa et al., 2007). The cannula was placed into the NAc (1.4 mm anterior and 0.6 mm lateral from bregma, 4.2 mm below skull surface) according to the atlas (Paxions and Franklin, 2008). The next day after surgery, a dialysis probe (AI-4-1; 1 mm membrane length, EICOM) was inserted through a guide cannula and perfused with a ringer's solution (147 mM NaCl, 4 mM KCl, 2.3 mM $CaCl_2$) at a flow rate of 0.5 μl/min by a syringe pump (ESP-64, EICOM). Dialysate was collected in 15 min fraction and injected into the HPLC system (HTEC-500, EICOM) to quantitate extracellular DA levels. Three samples were used to establish baseline levels of extracellular DA.

Measurement of NAA and NAAG

The measurement of NAA and NAAG by HPLC was performed as described previously (Reynolds et al., 2005; Takanashi et al., 2012). Brain tissue was homogenized with 10 times the volume of 0.1 M perchloric acid. We applied the solution to pretreated SPEC 3 ml SAX 15 mg anion exchange columns for NAc (Agilent Technologies, USA) followed by extraction with 5.88 ml/l phosphate acid (85%). Samples were injected into the HPLC system (LC-2010CHT, Shimadzu, Japan) with ZORBAX SB-C18 columns (4.6×250 mm, Agilent Technologies). The detector was set at 215 nm. NAA and NAAG peaks in the sample were identified by their retention times compared to standards. Both NAA and NAAG gave linear standard curve and the compounds were quantified using peak height measurements.

Statistical analysis

All data are expressed as the mean±S.E.M. Statistical differences between the two groups were determined with a Student-*t* test. Statistical differences among values for individual groups were determined by analysis of variance (ANOVA), followed by the Student–Newmann–Keuls *post-hoc* test, when *F* ratios were significant ($p<0.05$). In the analysis of the development of locomotor sensitization and *in vivo* microdialysis, statistical differences were determined by ANOVA with repeated measurement, followed by Bonferroni's *post-hoc* test (Prism version 5).

Results

Microinjection of AAV-Shati vector enhanced the expression levels of Shati/Nat8l mRNA in the NAc and dS

AAV vector containing only EGFP (Mock) or both Shati and EGFP (Shati) sequences (Fig. 1*a*) were injected into the NAc (Fig. 1*b* left) (NAc-Mock and NAc-Shati, respectively) or dS (Fig. 1*b* right) (dS-Mock and dS-Shati, respectively) of mice. Shati/Nat8l mRNA expression levels were measured by quantitative RT-PCR and were presented as relative to the expression of *36B4*, the internal control (Krzyzosiak et al., 2010). Shati/Nat8l mRNA levels increased 7.0±0.69 fold in the NAc of NAc-Shati mice compared with that of NAc-Mock mice (Fig. 1*c*; left two columns). No change was observed in the dS (Fig. 1*c*; right two columns). On the other hand, Shati/Nat8l mRNA was elevated 13±1.9 fold only in the dS of dS-Shati mice compared with that of dS-Mock mice (Fig. 1*d*). As shown in both left upper panels of Fig. 1*e* and *f*, Shati/Nat8l mRNA was also detected by *in situ* hybridization in the NAc and dS, respctively. However, the Mock-injected site showed little detectable Shati/Nat8l mRNA (both left lower panels of Fig. 1*e* and *f*). Moreover, immunohistochemistry revealed that there was obvious protein expression of EGFP in the AAV vector injection site of the NAc and dS (both right panels of Fig. 1*e* and *f*).

Overexpression of Shati/Nat8l in the NAc reduced METH-induced hyperlocomotion

Figure 2*a* and *b* show locomotor activity induced by a single METH treatment (1.0 mg/kg s.c.) in mice. In Fig. 2*a*, both NAc-Mock and NAc-Shati mice exhibited METH-induced hyperlocomotion. However,

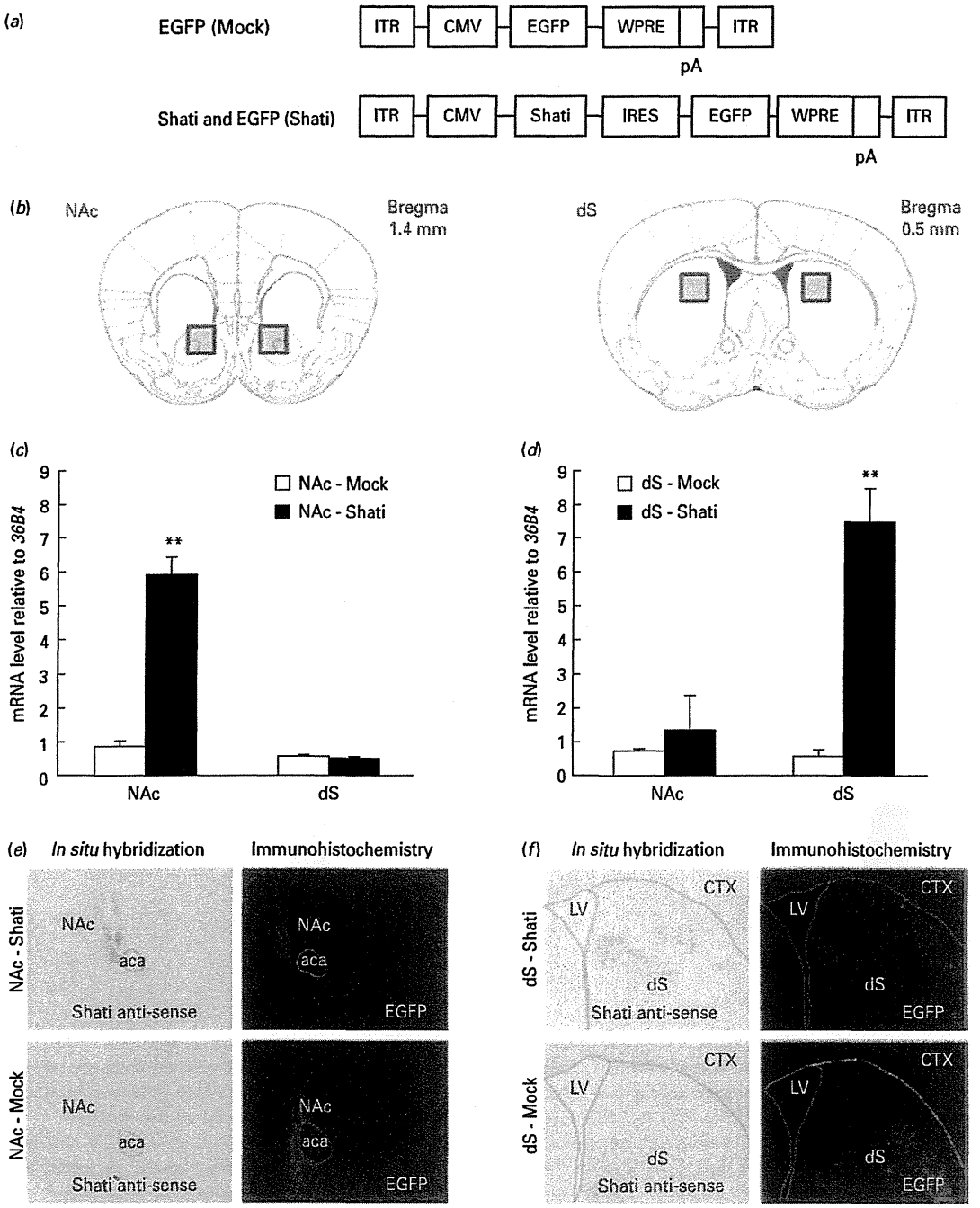

Fig. 1. Schematic representation of the AAV vector and effect of AAV-Shati vector microinjection in the NAc or dS. (*a*) Sequence of AAV-Mock or -Shati vector. An AAV vector was constructed using the cytomegalovirus immediate-early promoter (CMV) to drive EGFP or Shati. ITR: inverted terminal repeats; IRES: internal ribosomal entry site; WRPE: woodchuck hepatitis virus post-transcriptional regulatory element; pA: polyadenylation signal sequences. (*b*) Microinjection site of AAV-Mock or -Shati vector. The square insertions illustrate the brain region that was injected with each AAV vector. (*c, d*) Expression levels of Shati/Nat8l mRNA in the NAc-Shati (*c*) or dS-Shati (*d*) mice. For each group N=3. $^{**}p<0.01$ *vs.* each Mock group (Student-*t* test). (*e, f*) *In situ* hybridization for Shati/Nat8l mRNA and immunohistochemical staining for representative EGFP in the NAc-Shati (*e*) or dS-Shati (*f*) mice. aca: anterior commissure; LV: lateral ventricle; CTX: cortex.

METH-induced hyperlocomotion in NAc-Shati mice was decreased significantly compared with that in NAc-Mock mice ($F_{3,33}$=43.16, p<0.0001). On the other hand, there were no differences of METH-induced locomotor activities between dS-Shati and dS-Mock mice (Fig. 2*b*).

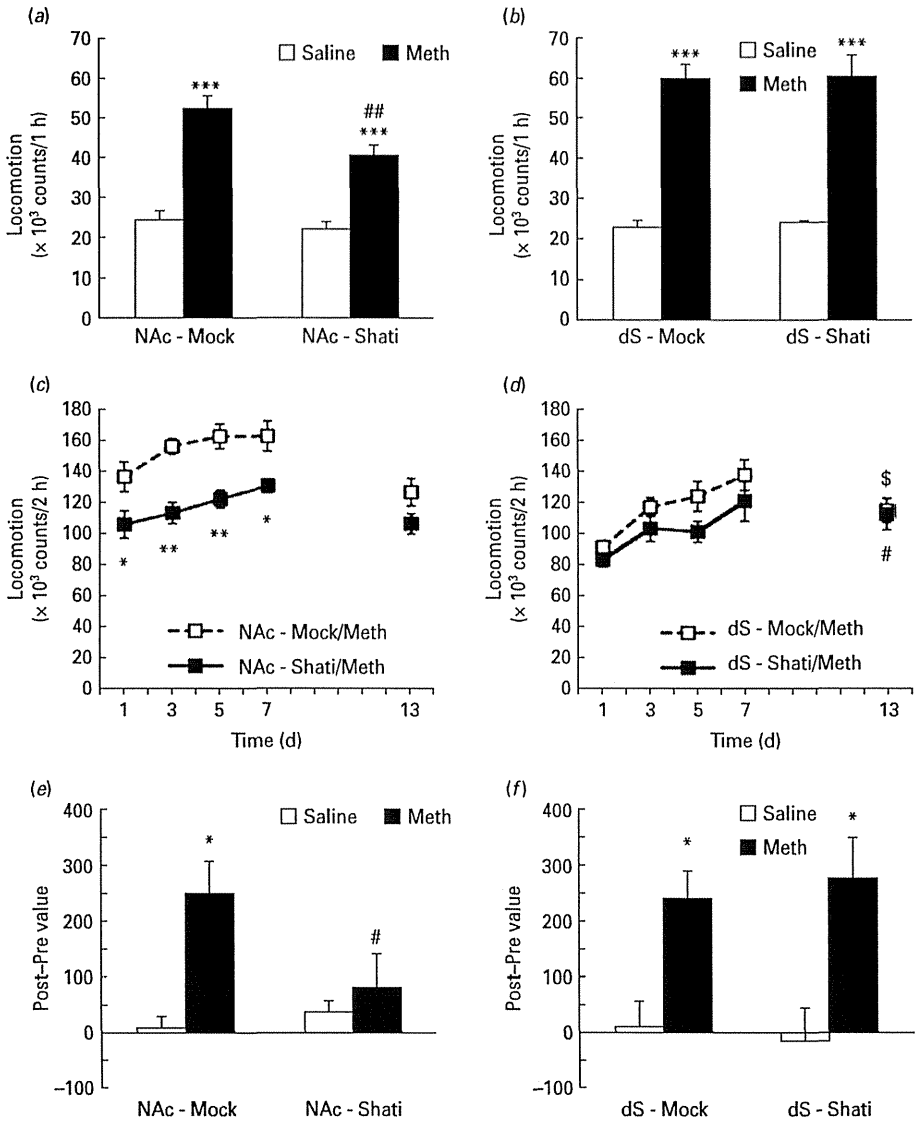

Fig. 2. Effect of overexpression of Shati/Nat8l in the NAc or dS on METH-induced behavioral alterations. (*a, b*) METH-induced locomotor activity in the NAc-Shati (*a*) or dS-Shati (*b*) mice. Saline or METH (1 mg/kg, s.c.) was administered immediately before the measurement of locomotor activity for 60 min. For NAc-Mock $N=8$, NAc-Shati $N=9$, dS-Mock $N=8$, dS-Shati $N=9$. $^{***}p<0.001$ *vs.* corresponding saline treatment group, $^{\#\#}p<0.01$ *vs.* METH-treated NAc-Mock group (ANOVA followed by the Student–Newman–Keuls *post-hoc* test). (*c, d*) METH-induced locomotor sensitization in the NAc-Shati (*c*) or dS-Shati (*d*) mice. For NAc-Mock $N=5$, NAc-Shati $N=5$, dS-Mock $N=5$, dS-Shati $N=7$. $^{*}p<0.05$, $^{**}p<0.01$ *vs.* METH-treated NAc-Mock group. $^{\$}p<0.05$ *vs.* locomotor activity on Day 1 of METH-treated dS-Mock group. $^{\#}p<0.05$ *vs.* locomotor activity on Day 1 of METH-treated dS-Shati group (ANOVA with repeated measures followed by the Bonferroni's *post-hoc* test, ANOVA followed by the Student–Newman–Keuls *post-hoc* test). (*e, f*) METH-induced conditioned place preference in the NAc-Shati (*e*) or dS-Shati (*f*) mice. For each group $N=9$. $^{*}p<0.05$ *vs.* corresponding saline treatment group, $^{\#}p<0.05$ *vs.* METH-treated NAc-Mock group (ANOVA followed by the Student–Newman–Keuls *post-hoc* test).

Overexpression of Shati/Nat8l in the NAc reduced METH-induced locomotor sensitization

We examined the efficacy of overexpression of Shati/Nat8l on locomotor sensitization induced by repeated METH treatments. Mice were administrated METH (1 mg/kg/day, s.c. for 7 d) and were re-challenged with a lower dose of METH (0.3 mg/kg, s.c.) on Day 13 after withdrawal for 5 d. Locomotor activity was measured for 2 h on Day 1, 3, 5, 7, and 13. In Fig. 2*c*, daily METH treatment for 7 d caused a sensitization to the locomotor-stimulating effects in NAc-Mock ($F_{3,12}=4.814$, $p<0.05$) and NAc-Shati mice ($F_{3,12}=13.42$, $p<0.001$). Although there was no significant difference between NAc-Mock and NAc-Shati mice in the time course of locomotor sensitization (AAV vector treatment, $F_{1,8}=16.22$, $p<0.01$: time, $F_{3,24}=12.38$,

$p<0.0001$: AAV vector treatment × time, $F_{3,24}=0.92$, $p=0.4467$), METH-induced hyperlocomotion was significantly reduced in NAc-Shati mice compared with NAc-Mock mice on Day 1, 3, 5 and 7. Also in both dS-Mock ($F_{3,12}=19.82$, $p<0.0001$) and dS-Shati mice ($F_{3,18}=8.562$, $p<0.01$), repeated administration of METH resulted in the development of locomotor sensitization (Fig. 2*d*). There was no significant difference in the time course of METH-induced sensitization between dS-Mock and dS-Shati mice on Day 1–7 (AAV vector treatment, $F_{1,10}=3.39$, $p=0.0953$: time, $F_{3,30}=8.60$, $p<0.0001$: AAV vector treatment × time, $F_{3,30}=1.59$, $p=0.2121$). In NAc-Mock and NAc-Shati mice, locomotor activity after re-challenge METH treatment on Day 13 was not decreased compared with Day 1 ($F_{3,16}=3.212$, $p=0.0512$), although the challenge dose of METH was lower than the daily dose. Both dS-Mock and dS-Shati mice showed locomotor sensitization after re-challenge with METH on Day 13 ($F_{3,20}=5.608$, $p<0.01$), but there was no difference in locomotor activity of dS-Mock and dS-Shati mice on Day 13.

Overexpression of Shati/Nat8l in the NAc reduced METH-induced CPP

As shown in Fig. 2*e*, METH treatment produced place preference in NAc-Mock mice in the place conditioning paradigm. However, the preferred effect of METH in NAc-Shati mice was significantly weaker than that in NAc-Mock mice ($F_{3,15}=5.412$, $p<0.05$). On the other hand, the administration of METH induced CPP in both dS-Shati and dS-Mock mice, and there was no difference in the preferred effect of METH between these groups (Fig. 2*f*) ($F_{3,16}=7.039$, $p<0.01$).

The behavioral alterations in locomotor activity, locomotor sensitization and CPP described above indicate that the overexpression of Shati/Nat8l in the NAc, but not in the dS, suppressed METH-induced addictive behaviors.

Overexpression of Shati/Nat8l in the NAc suppressed the basal levels of extracellular DA and METH-induced elevation of extracellular DA levels

To clarify the suppressive mechanism of Shati/Nat8l overexpression in the NAc, but not in the dS, for METH-induced behavioral alterations in mice, we measured the METH-induced elavation of extracellular DA levels in the NAc of NAc-Mock or NAc-Shati mice using an *in vivo* microdialysis method.

Basal levels of extracellular DA in the NAc of NAc-Shati mice were significantly lower than that of NAc-Mock mice (Fig. 3*a*) (NAc-Mock mice, 1.39±0.33 nM: NAc-Shati mice, 0.28±0.07 nM). METH (1 mg/kg, s.c.)-induced DA elevation was markedly suppressed in the NAc of NAc-Shati mice compared with that of NAc-Mock mice (Fig. 3*b*) (AAV vector treatment, $F_{1,10}=35.35$, $p<0.001$: time, $F_{11,66}=34.14$, $p<0.0001$: AAV vector treatment × time, $F_{11,66}=9.423$, $p<0.0001$). The increase of extracellular DA levels by METH was observed in both NAc-Shati ($F_{9,27}=7.121$, $p<0.0001$) and NAc-Mock ($F_{9,27}=22.18$, $p<0.0001$) mice (Fig. 3*b*). The peak of extracellular DA levels was elevated to over 150 and 260% of the baseline levels in the NAc-Shati and NAc-Mock mice, respectively, by a single METH treatment (Fig. 3*b*).

Overexpression of Shati/Nat8l in the NAc increased the tissue contents of NAA and NAAG

Since Shati/Nat8l synthesizes NAA and its NAA is condensed with glutamate to produce NAAG in the brain, we measured the tissue contents of NAA and NAAG in the NAc by HPLC method. The tissue contents of NAA and NAAG in the NAc are shown in Fig. 3*c* and *d*, respectively. Both NAA and NAAG levels in the NAc of NAc-Shati mice were significantly higher than those of NAc-Mock mice. However, there were no differences in tissue contents of NAA and NAAG in the dS between NAc-Shati and NAc-Mock mice (data not shown).

The suppressive effect of Shati/Nat8l overexpression in the NAc on METH-induced behavioral alterations was inhibited by the selective group II mGluRs antagonist

We examined the involvement with group II mGluRs on attenuated METH-induced behavioral alterations in the NAc-Shati mice, using the selective group II mGluRs antagonist LY341495. Figure 4*a* shows that pretreatment with LY341495 (0.1 mg/kg, i.p.) 30 min prior to METH treatment blocked the suppressive effect of Shati/Nat8l overexpression in the NAc on METH-induced hyperlocomotion ($F_{5,43}=16.85$, $p<0.0001$). Furthermore, the suppressive effect of Shati/Nat8l overexpression on METH-induced CPP was blocked by the same pretreatment with LY341495 (Fig. 4*b*, $F_{5,50}=4.443$, $p=0.0020$).

The suppressive effect of Shati/Nat8l overexpression in the NAc on METH-induced DA elevation was inhibited by the selective group II mGluRs antagonist

Next, we investigated the suppressive mechanism of Shati/Nat8l overexpression for attenuating the METH-induced elevation of extracellular DA levels in the NAc. In this experiment, we also used the selective group II mGluRs antagonist LY341495. Figure 4*c* shows that pretreatment with LY341495 (0.1 mg/kg, i.p.) 30 min prior to METH treatment blocked the suppressive effect of Shati/Nat8l overexpression in the NAc on METH-induced DA elevation. Therefore, two-way ANOVA with repeated measures did not reveal significant differences between NAc-Shati and NAc-Mock mice (AAV vector treatment, $F_{1,10}=0.6003$, $p=0.4679$: time, $F_{11,66}=29.22$, $p<0.0001$: AAV vector treatment × time, $F_{11,66}=1.217$, $p=0.2937$). Alternatively, pretreatment with 0.1 mg/kg LY341495 did not affect the METH-induced elevation of extracellular DA levels in the NAc of AAV vector non-injected mice (wild-type

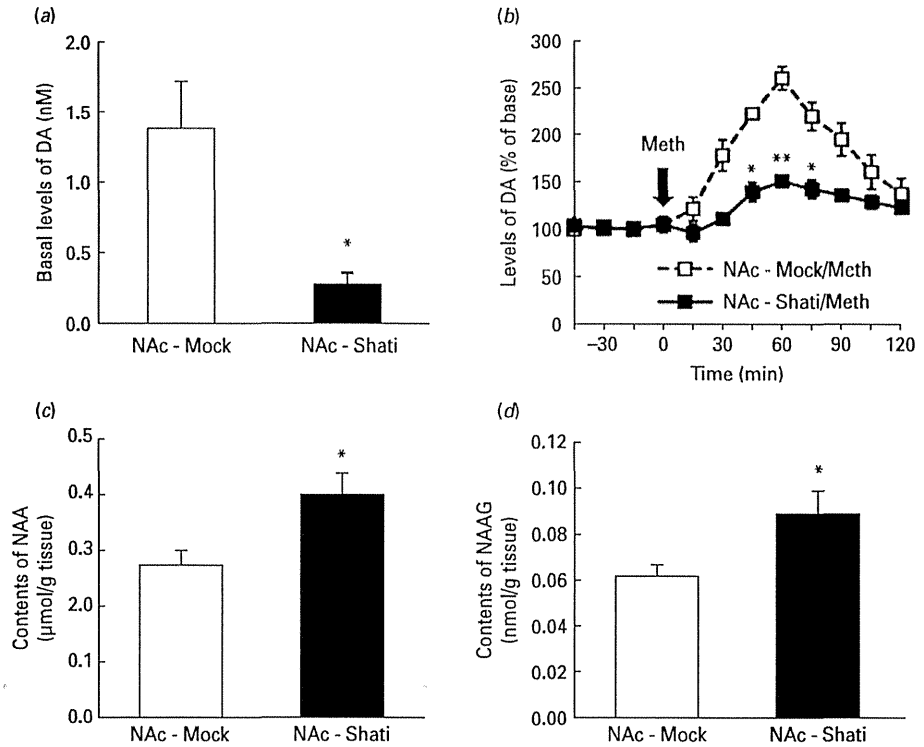

Fig. 3. Effect of overexpression of Shati/Nat8l in the NAc on basal levels of extracellular DA and tissue contents of NAA and NAAG. (*a*) Basal levels of extracellular DA in the NAc of Nac-Shati mice. For each group $N=9$. $^{*}p<0.05$ *vs.* NAc-Mock group (Student-*t* test). (*b*) METH-induced elevation of extracellular DA levels in the NAc of NAc-Shati mice. For each group $N=9$. $^{***}p<0.001$ *vs.* METH-treated NAc-Mock group (ANOVA with repeated measures followed by the Bonferroni's *post-hoc* test). (C, D) Tissue contents of NAA (*c*) and NAAG (*d*) in the NAc of NAc-Shati mice. For NAc-Mock $N=7$, NAc-Shati $N=6$. $^{*}p<0.05$ *vs.* NAc-Mock group (Student-*t* test).

mice) (Fig. 3*d*). Furthermore, in wild-type mice, pretreatment with the higher dose of LY341495 (0.3 mg/kg) markedly increased the METH-induced elevation of extracellular DA levels (Fig. 3*d*).

The elevation of NAAG reduced the basal levels of extracellular DA and METH-induced elevation of extracellular DA levels in the NAc

NAAG is known as a highly selective agonist of mGluR3 (Neale et al., 2000). We used 2-PMPA, the selective glutamate carboxypeptidase II (GCP II) inhibitor, to prevent the degradation of endogenous NAAG. Figure 4*e* shows that the basal levels of extracellular DA were obviously decreased by the administration of 2-PMPA (30 mg/kg, i.p.) in the NAc of wild-type mice ($F_{8,16}=35.01$, $p<0.0001$). Next, we perfused NAAG (0.1 mg/ml, 15 min) through the *in vivo* microdialysis probe in the NAc of wild-type mice. As shown in Fig. 4*f*, intra-NAc perfusion of NAAG significantly reduced the basal levels of extracellular DA in the NAc ($F_{8,16}=10.74$, $p<0.0001$). Therefore, both pretreatment with 2-PMPA and preperfusion of NAAG into the NAc attenuated METH-induced elevation of extracellular DA levels in the NAc (Fig. 4*e* and *f*).

These observations in aforementioned assays suggest that the elevation of NAAG induced by Shati/Nat8l overexpression in the NAc attenuates the METH-induced elevation of extracellular DA levels via activation of mGluR3, one of the group II mGluRs.

Discussion

METH addiction is mediated by multiple brain regions, neurotransmitter systems and bioactive molecules. In the present study, we clarified differential roles of Shati/Nat8l, a novel aspartate *N*-acetyltransferase, in the NAc and dS. Our results suggest that Shati/Nat8l in the NAc mediates METH-induced behavioral and dopaminergic neuronal responses via activation of group II mGluRs.

The AAV vector is a noteworthy gene delivery tool for therapeutic approaches to neurological diseases, and the safety of this vector for clinical use in the human brain has been confirmed (Muramatsu et al., 2010; Miyazaki et al., 2012). The transfer of AAV vector is stable and long-term gene expression can be attained in neuronal function (Eberling et al., 2009). The AAV vector transduces neurons preferentially, but not glial cells (Davidson et al., 2000; Tenenbaum et al., 2004). Therefore, we used

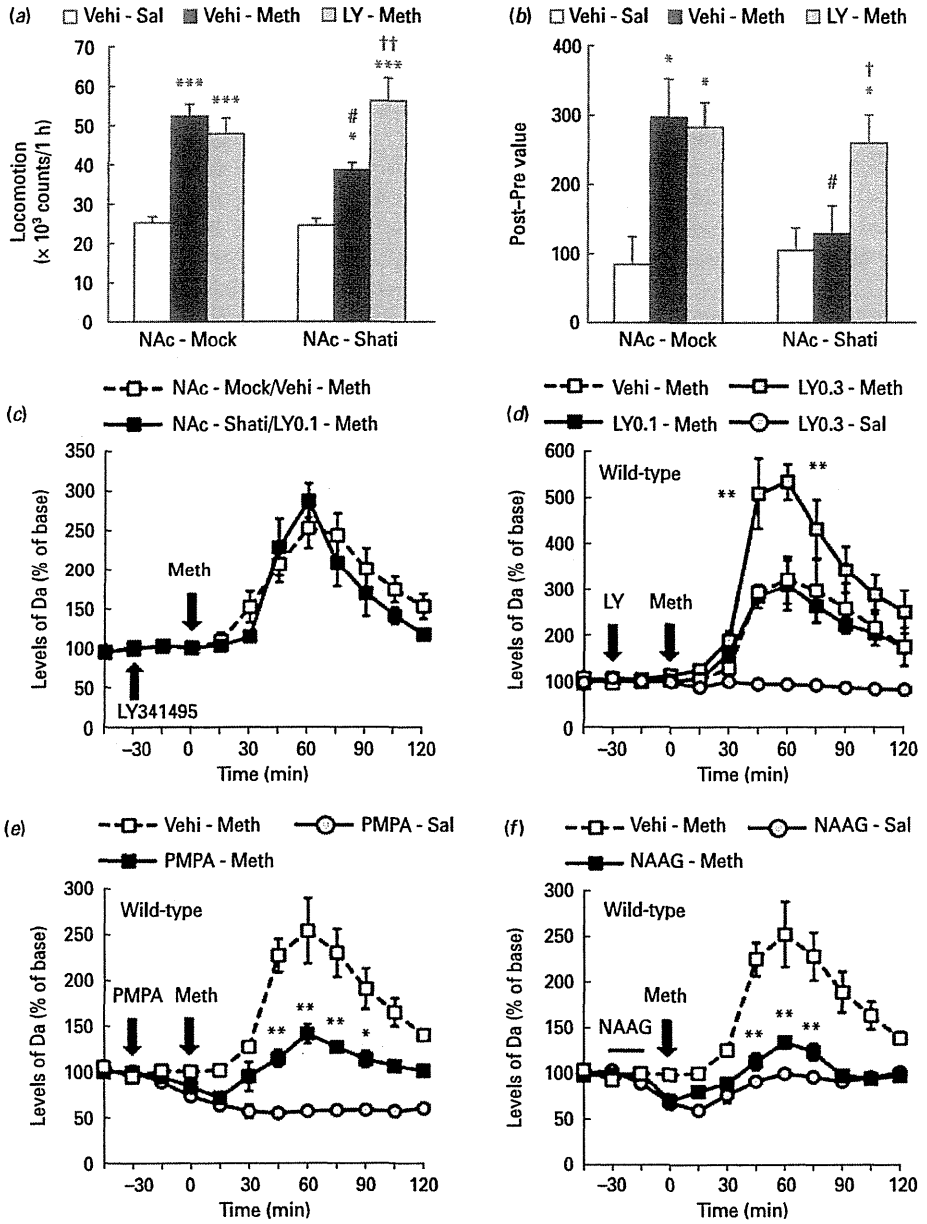

Fig. 4. Effect of group II mGluRs antagonist on METH-induced alterations in the NAc-Shati mice and effect of 2-PMPA and NAAG on METH-induced elevation of extracellular DA levels in the NAc in mice. (*a, b*) Effect of group II mGluRs antagonist on METH-induced locomotor activity (*a*) and conditioned place preference (*b*) in the NAc-Shati mice. Pretreatment with LY341495 (0.1 mg/kg, i.p. 30 min prior to METH treatment) canceled attenuated METH-induced behavioral alterations in the NAc-Shati mice. For each group, $N=9$. $^{*}p<0.05$, $^{***}p<0.001$ *vs.* corresponding vehicle–saline treatment group, $^{\#}p<0.05$ *vs.* vehicle–METH-treated NAc-Mock group, $\dagger p<0.05$, $\dagger\dagger p<0.01$ *vs.* vehicle–METH-treated NAc-Shati group (ANOVA followed by the Student–Newman–Keuls *post-hoc* test). (*c*) Effect of group II mGluRs antagonist on METH-induced elevation of extracellular DA in NAc-Shati mice. Pretreatment with LY341495 (0.1 mg/kg, *i.p.* 30 min prior to METH treatment) canceled attenuated METH-induced elevation of extracellular DA in the NAc of NAc-Shati mice. For each group $N=4$. ANOVA with repeated measures did not reveal significant differences between NAc-Mock and NAc-Shati mice. (*d*) Effect of group II mGluRs antagonist on METH-induced elevation of extracellular DA in the normal (none-AAV-injected) mice. Pretreatment with LY341495 (0.3 mg/kg, i.p. 30 min prior to METH treatment) enhanced METH-induced elevation of extracellular DA in the NAc of normal mice. For each group, $N=5$. $^{**}p<0.01$ *vs.* vehicle–METH treatment group (ANOVA with repeated measures followed by the Bonferroni's *post-hoc* test). (*e, f*) Effect of GCP II inhibitor (*e*) and exogenous NAAG (*f*) on METH-induced elevation of extracellular DA in the wild-type mice. Pretreatment with 2-PMPA (30 mg/kg, i.p. 30 min prior to METH treatment) (*e*) and NAAG perfusion (0.1 mg/ml, 15 min) (*f*) inhibited METH-induced elevation of extracellular DA in the NAc of wild-type mice. For each group $N=4$. $^{*}p<0.05$, $^{**}p<0.01$ *vs.* vehicle–METH treatment group. (ANOVA with repeated measures followed by the Bonferroni's *post-hoc* test).

AAV vector to overexpress Shati/Nat8l in the mouse brain. The AAV-Shati vector injection induced the expression of Shati/Nat8l mRNA in the NAc or dS specifically, as assessed by quantitative real-time RT-PCR and *in situ* hybridization methods (Fig. 1*c–f*). In addition, this injection also enhanced the tissue contents of NAA in the NAc (Fig. 3*c* and *d*). Thus, it seems the inducible Shati/Nat8l by AAV vector injection possessed *N*-acetyltransferase activity for aspartate, at least in the NAc.

The psychostimulant, METH, causes hyperlocomotion in rodents (Kitanaka et al., 2005). METH-induced enhancement of locomotor activity was suppressed significantly in the NAc-Shati mice (Fig. 2*a*). Repeated treatments of METH can produce behavioral sensitization in rodents, characterized by a progressively enhanced locomotor activity (Shen et al., 2010). On Days 1–7 during METH treatments, METH-induced hyperlocomotion was reduced in the NAc-Shati mice (Fig. 2*c*). METH-induced CPP in mice is a popular model of drug-mediated associative learning in humans (Shen et al., 2006). In the CPP task, the potentiation of place preference by METH was not observed in the NAc-Shati mice (Fig. 2*e*). These results showed that the overexpression of Shati/Nat8l in the NAc inhibits METH-induced behaviors in mice. METH-induced hyperlocomotion and CPP are closely related to the activation of the dopaminergic system (Kim and Jang, 1997; Wakuda et al., 2008). The efficacy of METH depends primarily on its ability to increase extracellular DA levels in the brain (Clarke et al., 1988; Kuczenski et al., 1995; Goodwin et al., 2009). In this study, the METH-induced elevation of extracellular DA levels was significantly suppressed in the NAc of NAc-Shati mice (Fig. 3*b*). Thus, our results demonstrate that the attenuation of METH-induced behavioral alterations by Shati/Nat8l overexpression occurs via suppressing the increase of extracellular DA levels in the NAc.

Overexpression of Shati/Nat8l enhanced the tissue contents of not only NAA (Fig. 3*c*) but also NAAG (Fig. 3*d*) in the NAc. NAAG is synthesized by a NAAG synthetase catalyzing the ATP-dependent condensation of NAA and glutamate (Becker et al., 2010), and is the most widely abundant distributed peptide neurotransmitter in mammalian neurons (Neale et al., 2005). It was also found to be a highly selective endogenous mGluR3 agonist (Wroblewska et al., 1997). Group II mGluRs including mGluR2 and 3 are coupled G_i proteins, which negatively regulate adenylate cyclase activity, and are expressed at moderate-to-high levels in brain regions implicated in drug addiction (Adewale et al., 2006). Pretreatment with the group II mGluRs antagonist LY341495 attenuated the suppressive effect of Shati/Nat8l overexpression on the METH-induced locomotor activity (Fig. 4*a*), CPP (Fig. 4*b*) and elevation of extracellular DA levels (Fig. 4*c*). The elevation of endogenous NAAG by its peptidase inhibitor, 2-PMPA, in naive mice resulted in a reduction in the basal levels of extracellular DA in the NAc (Fig. 4*e*). Moreover, exogenous NAAG perfusion significantly decreased the basal levels of extracellular DA in the NAc of naive mice (Fig. 4*f*). The mechanism underlying the regulation of the dopaminergic system by NAAG and mGluR3 is not fully understood. Previously, it was demonstrated that 2-PMPA lowered the basal levels of extracellular glutamate in the NAc of rats, and the effect was blocked by pretreatment with LY341495 (Xi et al., 2010). The NAc receives glutamatergic neuronal afferents from the prefrontal cortex, hippocampus and amygdala (Meredith et al., 1993), and these afferents increase DA release in the NAc (Taber and Fibiger, 1995; Chaki et al., 2006). Therefore, the activation of mGluR3 by NAAG could inhibit glutamate release from the terminals of glutamatergic afferents, which in turn reduces DA release in the NAc. Taken together, these results suggest that Shati/Nat8l may reduce indirectly the basal levels of extracellular DA by elevating NAAG, a selective endogenous mGluR3 agonist. This speculation is supported by the observation that the basal levels of extracellular DA were decreased significantly by 20% in the NAc of NAc-Shati mice (Fig. 3*a*), which enhanced the tissue contents of NAAG in the NAc.

Another important finding of this study was the regional specificity of the functional contribution of Shati/Nat8l in the brain. Curiously, although the expression levels of Shati/Nat8l mRNA were increased in both the dS of dS-Shati mice and the NAc of NAc-Shati mice, the overexpression of Shati/Nat8l in the NAc, but not in the dS, suppressed METH-induced abnormal behaviors. This discrepancy may be attributed to the distribution of several enzymes and amino acids involved with the functional role of Shati/Nat8l. Shati/Nat8l catalyzes the *N*-acetylation of aspartate to produce NAA, and then NAAG is synthesized from NAA and glutamate by NAAG synthetase I in the cytoplasm (Becker et al., 2010; Neale et al., 2011). NAAG is released from nerve terminals, most likely via synaptic vesicles, although the transporter into synaptic vesicles for NAAG has not been identified. Released NAAG binds to mGluR3 on the presynaptic membranes (Conn and Pin, 1997), and is also degraded by GCP II (Becker et al., 2010), liberating NAA and glutamate (Moffett, et al., 2007). Liberated NAA is translated into astrocytes and oligodendrocytes by sodium-dependent dicarboxylate (NaDC3). Another glutamate liberated by GCP II modulates glutamatergic neurotransmission (Zhou et al., 2005). The next step is to identify differences in the distribution of aspartate, glutamate, NAAG synthetase I, GCP II, and NaDC3 between in the NAc and dS, and to clarify the functional contribution of NAAG to the dopaminergic system in each brain region.

In conclusion, we hypothesize that the expression of Shati/Nat8l in the NAc inhibits METH-induced elevation in the extracellular levels of DA via mediating NAAG and mGluR3. As a result of the suppression on the extracellular levels of DA in the NAc, Shati/Nat8l inhibits

METH-induced hyperlocomotion and CPP. Since the NAc and dS are involved in A10 and A9 neuronal cell groups, respectively, the different role of Shati/Nat8l between the NAc and dS may be dependent on distinct neuronal regulation in these cell groups. We need further study, but the difference could be a new key point to clarify the mechanisms of drug addiction. Thus, we provide evidence that Shati/Nat8l in the NAc is a key molecule to suppress METH-induced abnormal behaviors by mediating extracellular DA levels via activation of grop II mGluRs, probably of mGluR3. Moreover, the Shati/Nat8l-related neuronal system may become a new target of therapy for METH addiction.

Acknowledgment

We thank Naomi Takino, Hitomi Miyauchi, and Keiko Ayabe for technical assistance in producing the AAV vectors, and Kohichi Tanaka and Yukiko Ito (Department of Molecular Neuroscience Medical Research Institute, School of Biomedical Science Tokyo Medical and Dental University, Tokyo, Japan) for technical support of the measurement of NAA and NAAG.

Funding

This study was supported by a Program for Next Generation World-Leading Researchers (LS047), grants-in-aid for Scientific Research from Japan Society for the Promotion of Science, a grant-in-aid for Research on Regulatory Science of Pharmaceuticals, Health and Labour Science Research Grants from the Ministry of Health, Labour and Welfare of Japan, a grant-in-aid from the research committee of CNS degenerative diseases of the Ministry of Health, Labour and Welfare of Japan, a grant-in-aid for scientific research on innovative areas (Synapse Neurocircuit Pathology) from the Ministry of Education, Culture, Sports, Science and Technology of Japan, and a SRF Grant for Biomedical Research.

Statement of Interest

None.

References

Adewale AS, Platt DM, Spealman RD (2006) Pharmacological stimulation of group ii metabotropic glutamate receptors reduces cocaine self-administration and cocaine-induced reinstatement of drug seeking in squirrel monkeys. J Pharmacol Exp Ther 318:922–931.

Ariyannur PS, Moffett JR, Manickam P, Pattabiraman N, Arun P, Nitta A, Nabeshima T, Madhavarao CN, Namboodiri AM (2010) Methamphetamine-induced neuronal protein NAT8L is the NAA biosynthetic enzyme: implications for specialized acetyl coenzyme A metabolism in the CNS. Brain Res 1335:1–13.

Beauvais G, Atwell K, Jayanthi S, Ladenheim B, Cadet JL (2011) Involvement of dopamine receptors in binge methamphetamine-induced activation of endoplasmic reticulum and mitochondrial stress pathways. PLoS One 6: e28946. doi: 10.1371/journal.pone.0028946.

Becker I, Lodder J, Gieselmann V, Eckhardt M (2010) Molecular characterization of *N*-acetylaspartylglutamate synthetase. J Biol Chem 285:29156–29164.

Chaki S, Yoshikawa R, Okuyama S (2006) Group II metabotropic glutamate receptor-mediated regulation of dopamine release from slices of rat nucleus accumbens. Neurosci Lett 404:182–186.

Clarke PB, Jakubovic A, Fibiger HC (1988) Anatomic analysis of the involvement of mesolimbocortical dopamine in the locomotor stimulant actions of D-amphetamine and apomorphine. Psychopharmacol 96:511–520.

Conn PJ, Pin JP (1997) Pharmacology and functions of metabotropic glutamate receptors. Annu Rev Pharmacol Toxicol 37:205–237.

Davidson BL, Stein CS, Heth JA, Martins I, Kotin RM, Derksen TA, Zabner J, Ghodsi A, Chiorini JA (2000) Recombinant adeno-associated virus type 2, 4, and 5 vector: transduction of variant cell types and regions in the mammalian central nervous system. Proc Natl Acad Sci USA 97:3428–3432.

Di Ciano P, Robbins TW, Everitt BJ (2008) Differential effects of nucleus accumbens core, shell, or dorsal striatal inactivations on the persistence, reacquisition, or reinstatement of responding for a drug-paired conditioned reinforcer. Neuropsychopharmacol 33:1413–1425.

Eberling JL, Kells AP, Pivirotto P, Beyer J, Bringas J, Federoff HJ, Forsayeth J, Bankiewicz KS (2009) Functional effects of AAV2-GDNF on the dopaminergic nigrostriatal pathway in parkinsonian rhesus monkeys. Hum Gene Ther 20:511–518.

Everitt BJ, Robbins TW (2005) Neural systems of reinforcement for drug addiction: from actions to habits to compulsion. Nat Neurosci 8:1481–1489.

Furukawa-Hibi Y, Nitta A, Fukumitsu H, Somiya H, Furukawa S, Nabeshima T, Yamada K (2010) Overexpression of piccolo C2A domain induces depression-like behavior in mice. Neuroreport 21:1177–1181.

Gerdeman GL, Partridge JG, Lupica CR, Lovinger DM (2003) It could be habit forming: drugs of abuse and striatal synaptic plasticity. Trends Neurosci 26:184–192.

Giros B, Jaber M, Jones SR, Wightman RM, Caron MG (1996) Hyperlocomotion and indifference to cocaine and amphetamine in mice lacking the dopamine transporter. Nature 379:606–612.

Goodwin JS, Larson GA, Swant J, Sen N, Javitch JA, Zahniser NR, De Felice LJ, Khoshbouei H (2009) Amphetamine and methamphetamine differentially affect dopamine transporters *in vitro* and *in vivo*. J Biol Chem 284:2978–2989.

Ikemoto S (2007) Dopamine rewardcircuitry: two projection systems from the ventral midbrain to the nucleus accumbens-olfactory tubercle complex. Brain Res Rev 56:27–28.

Kim HS, Jang CG (1997) MK-801 inhibits methamphetamine-induced conditioned place preference and behavioral sensitization to apomorphine in mice. Brain Res Bull 44:221–227.

Kitanaka T, Kitanaka J, Takemura M (2005) Inhibition of methamphetamine hyperlocomotion in mice by glorgyline, a

monoamine oxidase-A inhibitor, through alteration of the 5-hydroxytriptamine turnover in the striatum. Neuroscience 130:295–308.

Krzyzosiak A, Szyszka-Niagolov M, Wietrzych M, Gobaille S, Muramatsu S, Krezel W (2010) Retinoid x receptor gamma control of affective behaviors involves dopaminergic signaling in mice. Neuron 66:908–920.

Kuczenski R, Sgal DS, Cho AK, Melega W (1995) Hippocampus norepinephrine, caudate dopamine and serotonin, and behavioral responses to the stereoisomer of amphetamine and methamphetamine. J Neurosci 15:1308–1317.

Meredith GE, Pennartz CM, Groenewegen HJ (1993) The cellular framework for chemical signaling in the nucleus accumbens. Prog Brain Res 99:3–24.

Miyamoto Y, Yamada K, Nagai T, Mori H, Mishina M, Furukawa H, Noda Y, Nabeshima T (2004) Behavioural adaptations to addictive drugs in mice lacking the NMDA receptor epsilon1 subunit. Eur J Neurosci 19:151–158.

Miyazaki Y, Adachi H, Katsuno M, Minamiyama M, Jiang YM, Huang Z, Doi H, Matsumoto S, Kondo N, Iida M, Tohnai G, Tanaka F, Muramatsu S, Sobue G (2012) Viral delivery of miR-196a ameliorates the SBMA phenotype via the silencing of CELF2. Nat Med 18:1136–1141.

Moffett JR, Ross B, Arun P, Madhavarao CN, Namboodiri AM (2007) *N*-acetylaspartylglutamate in the CNS: from neurodiagnostics to neurobiology. Prog Neurobiol 81:89–131.

Muramatsu S, Fujimoto K, Kato S, Mizukami H, Asari S, Ikeguchi K, Kawakami T, Urabe M, Kume A, Sato T, Watanabe E, Ozawa K, Nakano I (2010) A phase 1 study of aromatic L-amino acid decarboxylase gene therapy for Parkinson's disease. Mol Ther 18:1731–1735.

Neale JH, Bzdega T, Wroblewska B (2000) *N*-acetylaspartylglutamate: the most abundant peptide neurotransmitter in the mammalian central nervous system. J Neurochem 75:443–452.

Neale JH, Olszewski RT, Gehl LM, Wroblewska B, Bzdega T (2005) The neurotransmitter *N*-acetylaspartylglutamate in models of pain, ALS, diabetic neuropathy, CNS injury and schizophrenia. Trends Pharmacol Sci 26:477–484.

Neale JH, Olszewsk RT, Zuo D, Janczura KJ, Profaci CP, Lavin KM, Madore JC, Bzdega T (2011) Advances in understanding the peptide neurotransmitter NAAG and appearance of a new member of the NAAG neuropeptide family. J Neurochem 118:490–498.

Nishikawa T, Mataga N, Takashima M, Toru M (1983) Behavioral sensitization and relative hyperresponsiveness of striatal and limbic dopaminergic neurons after repeated methamphetamine treatment. Eur J Pharmacol 88:195–203.

Nitta A, Ito M, Fukumitsu H, Ohmiya M, Ito H, Sometani A, Nomoto H, Furukawa Y, Furukawa S (1999) 4-Methlcatehol increases brain-derived neurotrophic factor content and mRNA expression in cultured brain cells and in rat bain *in vivo*. J Pharmacol Exp Ther 291:1276–1283.

Niwa M, Nitta A, Mizoguchi H, Ito Y, Noda Y, Nagai T, Nabeshima T (2007) A novel molecule 'Shati' is involved in methamphetamine-induced hyperlocomotion, sensitization, and conditioned place preference. J Neurosci 27:7604–7615.

Paxinos G and Franklin KBJ (2008) The mouse brain in stereotaxic coordinates. Compact 3rd edn. Amsterdam: Elsevier.

Reynolds LM, Cochran SM, Morris BJ, Pratt JA, Reynolds GP (2005) Chronic phencyclidine administration induces schizophrenia-like changes in *N*-acetylaspartate and *N*-acetylaspartylglutamate in rat brain. Schizophr Res 73:147–152.

Shen F, Meredith GE, Napier TC (2006) Amphetamine-induced place preference and conditioned motor sensitization requires activation of tyrosine kinase receptors in the hippocampus. J Neurosci 26:11041–11051.

Shen X, Purser C, Tien LT, Chiu CT, Paul IA, Baker R, Loh HH, Ho IK, Ma T (2010) μ-Opioid receptor knockout mice are insensitive to methamphetamine-induced behavioral sensitization. J Neurosci Res 88:2294–2302.

Sulzer D, Sonders MS, Poulsen NW, Galli A (2005) Mechanisms of neurotransmitter release by amphetamines: a review. Prog Neurobiolb 75:406–433.

Taber T, Fibiger HC (1995) Electrical stimulation of the prefrontal cortex increases dopamine release in the nucleus accumbens of the rat: modulation by metabotropic glutamate receptors. J Neurosci 15:3896–3904.

Takanashi J, Saito S, Aoki I, Barkovich AJ, Ito Y, Inoue K (2012) Increased *N*-acetylaspartate in model mouse of pelizaeus-merzbacher disease. J Magn Reason Imaging 35:418–425.

Tenenbaum L, Chtarto A, Lehtonen E, Velu T, Brotchi J, Levivier M (2004) Recombinant AAV-mediated gene delivery to the central nervous system. J Gene Med 6:212–222.

Wakuda T, Matsuzaki H, Suzuki K, Iwata Y, Shinmura C, Suda S, Iwata K, Yamamoto S, Sugihara G, Tsuchiya KJ, Ueki T, Nakamura K, Nakahara D, Takei N, Mori N (2008) Perinatal asphyxia reduces dentate granule cells and exacerbates methamphetamine-induced hyperlocomotion in adulthood. PLoS One 3:e3648. doi:10.1371/journal.pone.0003648.

Wroblewska B, Wrobleski JT, Pshenichkin S, Surin A, Sullivan SE, Sullivan SE, Neale JH (1997) *N*-acetylaspartylglutamate selectively activates mGluR3 receptors in transfected cells. J Neurochem 69:174–181.

Xi ZX, Li X, Peng XQ, Li J, Chun L, Gardner EL, Thomas AG, Slusher BS, Ashby CR Jr. (2010) Inhibition of NAALADase by 2-PMPA attenuates cocaine-induced relapse in rats: a NAAG-mGluR2/3-mediated mechanism. J Neurochem 112:564–576.

Zhou J, Neale JH, Pomper MG, Kozikowski AP (2005) NAAG peptidase inhibitors and their potential for diagnosis and therapy. Nat Rev Drug Discov 4:1015–1026.

Published online: December 15, 2014

Research Article

SOURCE DATA | TRANSPARENT PROCESS | OPEN ACCESS

EMBO Molecular Medicine

HMGB1 facilitates repair of mitochondrial DNA damage and extends the lifespan of mutant ataxin-1 knock-in mice

Hikaru Ito[1,†], Kyota Fujita[1,†], Kazuhiko Tagawa[1,†], Xigui Chen[1,‡], Hidenori Homma[1,‡], Toshikazu Sasabe[1], Jun Shimizu[2], Shigeomi Shimizu[3], Takuya Tamura[1], Shin-ichi Muramatsu[4] & Hitoshi Okazawa[1,5,*]

Abstract

Mutant ataxin-1 (Atxn1), which causes spinocerebellar ataxia type 1 (SCA1), binds to and impairs the function of high-mobility group box 1 (HMGB1), a crucial nuclear protein that regulates DNA architectural changes essential for DNA damage repair and transcription. In this study, we established that transgenic or virus vector-mediated complementation with HMGB1 ameliorates motor dysfunction and prolongs lifespan in mutant Atxn1 knock-in (Atxn1-KI) mice. We identified mitochondrial DNA damage repair by HMGB1 as a novel molecular basis for this effect, in addition to the mechanisms already associated with HMGB1 function, such as nuclear DNA damage repair and nuclear transcription. The dysfunction and the improvement of mitochondrial DNA damage repair functions are tightly associated with the exacerbation and rescue, respectively, of symptoms, supporting the involvement of mitochondrial DNA quality control by HMGB1 in SCA1 pathology. Moreover, we show that the rescue of Purkinje cell dendrites and dendritic spines by HMGB1 could be downstream effects. Although extracellular HMGB1 triggers inflammation mediated by Toll-like receptor and receptor for advanced glycation end products, upregulation of intracellular HMGB1 does not induce such side effects. Thus, viral delivery of HMGB1 is a candidate approach by which to modify the disease progression of SCA1 even after the onset.

Keywords AAV; DNA damage repair; HMGB1; mitochondria; SCA1
Subject Categories Genetics, Gene Therapy & Genetic Disease; Neuroscience
DOI 10.15252/emmm.201404392 | Received 2 July 2014 | Revised 11 November 2014 | Accepted 19 November 2014

Introduction

Spinocerebellar ataxia type 1 (SCA1) is one of the major groups of autosomal dominant hereditary cerebellar ataxia. The pathology shows dysfunctions and cell death of Purkinje cells in the cerebellum and motor neurons in the spinal cord. Correspondingly, patients show slowly progressive cerebellar ataxia, sometimes accompanied by neurogenic muscular atrophy mimicking motor neuron disease, and slow eye movement. The molecular mechanisms underlying the pathology have been gradually unravelled by extensive analyses by many groups. Importantly, overexpression of the normal form of the disease protein, ataxin-1 (Atxn1), has similar toxic effects on cells (Skinner *et al*, 1997), suggesting that an activity or interaction of mutant Atxn1, which normal Atxn1 also possesses, in excess causes neuronal dysfunction.

In this regard, the reciprocal interactions of Atxn1 with Capicua (CIC) and RNA binding motif protein 17 (RBM17) are of importance. Zoghbi's group and Orr's group found that mutant Atxn1 must be in its large native complexes to cause neurodegeneration and that its interactions with RBM17 are enhanced at the expense of interactions with CIC (Lam *et al*, 2006; Lim *et al*, 2008). Given that RBM17, also called splicing factor 45 (SPF45), is an RNA binding protein involved in splicing and that CIC/Capicua is a Sox2-like high-mobility group (HMG) protein involved in transcriptional repression, the shifted balance between splicing and transcription could broadly affect gene and protein expression profiles. We also found that polyglutamine binding protein 1 (PQBP1), a splicing factor involved in the U5 complex (Waragai *et al*, 2000; Zhang *et al*, 2000) at the step of exon–intron junction recognition by the spliceosome (Makarov *et al*, 2002; Makarova *et al*, 2004). It also binds to C-terminus of RNA polymerase II and similarly forms larger nuclear bodies through binding with Atxn1 (Okazawa *et al*, 2002), supporting the hypothesis that mutant Atxn1 shifted the balance of transcription and splicing to an abnormal state.

1 Department of Neuropathology, Medical Research Institute, Tokyo Medical and Dental University, Bunkyo-ku, Tokyo, Japan
2 Department of Neurology, The University of Tokyo, Bunkyo-ku, Tokyo, Japan
3 Department of Pathological Cell Biology, Medical Research Institute, Tokyo Medical and Dental University, Bunkyo-ku, Tokyo, Japan
4 Department of Neurology, Jichi Medical University, Shimotsuke, Tochigi, Japan
5 Center for Brain Integration Research, Tokyo Medical and Dental University, Bunkyo-ku, Tokyo, Japan
*Corresponding author. Tel: +81 3 5803 5847; E-mail: okazawa-tky@umin.ac.jp
†These authors contributed equally to this work
‡These authors contributed equally to this work

A current goal, therefore, is to find efficient methods to rescue the imbalance of gene expression and to determine the molecular mechanism that underlies the rescue. We previously searched for nuclear proteins quantitatively affected by mutant Atxn1 in neurons and found a significant decrease in high-mobility group box (HMGB) 1/2 proteins in the soluble nuclear fraction. The decrease was mainly attributed to proteasomal degradation and sequestration to inclusion bodies of the mutant Atxn1–HMGB1 complex (Qi *et al*, 2007). HMGB supplementation actually ameliorates eye degeneration in an SCA1 fly model and restores impaired DNA damage repair (Qi *et al*, 2007).

HMGB1/2 are architectural proteins that regulate the higher structure of genomic DNA. Consequently, they influence a broad range of nuclear functions, including transcription and DNA damage repair (Muller *et al*, 2001; Travers, 2003). HMGB1/2 possess HMG boxes like another Atxn1 binding partner, HMG-box transcription factor 1 (HBP1), which includes one Atxn1-HBP1 shared (AXH) domain (de Chiara *et al*, 2003) and one HMG box. The AXH domain may contribute to the self-association (Burright *et al*, 1997) or RNA binding (Yue *et al*, 2001) of Atxn1. These possibilities suggest that, in addition to architectural change of DNA, HMGB1 might influence the functional link between the HMG-box proteins (HBP1, Capicua, HMGB1/2) related to transcription and the AXH-domain proteins (Atxn1, HBP1) related to RNA metabolism.

In this study, we extend our previous findings in primary neurons and *Drosophila* and show that HMGB1 has a strong therapeutic effect on multiple phenotypes of mutant Atxn1-KI mice. In addition to the therapeutic effect of transgenic expression of HMGB1, we show that a single injection of an adeno-associated virus type 1 (AAV1) vector carrying HMGB1 is effective *in vivo* even after the onset of symptoms in mutant Atxn1-KI mice and that the therapeutic effect persists for more than 8 weeks. Moreover, we reveal mitochondrial DNA damage repair by HMGB1 as a new mechanism to rescue the pathology of SCA1.

Results

HMGB1 restores SCA1-KI mouse symptoms without affecting aggregation

We generated an HMGB1 transgenic mouse model on a C57BL/6 background expressing HMGB1 under the control of a 1.9-kb rat neuron-specific enhancer/promoter (Supplementary Fig S1A). Genome integration of the full-length construct was confirmed by PCR with genomic DNA from HMGB1-Tg mice (Supplementary Fig S1B). HMGB1 protein tagged with a 3× FLAG sequence was detected in total brain tissue by Western blot analysis (Supplementary Fig S1C) and in neurons of various brain regions including cerebral cortex, brain stem, hypothalamus and cerebellum by immunohistochemistry (Supplementary Fig S1D). In the cerebellum, expression of HMGB1-FLAG was prominent in Purkinje cells (Supplementary Fig S1E), which was confirmed by immunohistochemistry with anti-calbindin and anti-NeuN antibodies (Supplementary Fig S1F). HMGB1-Tg mice did not show pathological changes, such as decreased Purkinje cell number or decreased thickness of the molecular layer (Supplementary Fig S1G).

The major concern in the overexpression is that HMGB1 may trigger inflammatory responses via Toll-like receptor 2/4 (TLR2/4) or receptor for advanced glycation end products (RAGE) when released into the extracellular space (Park *et al*, 2006; Yu *et al*, 2006). Therefore, we tested inflammatory responses, including lymphocyte infiltration and microglia/macrophage activation, in the brains of HMGB1-Tg and non-Tg littermate mice (Supplementary Fig S2A). Peritoneal injection of lipopolysaccharide (LPS) into background mice (C57BL/6) was performed to make a positive control for brain inflammation. Immunohistochemistry of the cerebellum with antibodies against multiple inflammation marker proteins, such as CD4 (a helper T-cell marker), CD8 (a cytotoxic T-cell marker), CD11c (a dendritic cell marker) and microglial response factor-1 (a microglial marker), did not reveal any inflammation response in HMGB1-Tg mice (Supplementary Fig S2A). The cerebral cortex showed similar findings (data not shown). These results suggest that HMGB1 does not trigger brain inflammation in our mouse model (Supplementary Fig S1).

We next mated HMGB1-Tg mice with Atxn1-154Q knock-in mice (Atxn1-KI mice) of the same background C57BL/6 and generated double-transgenic mice (Atxn1-KI;HMGB1 mice). As reported previously (Qi *et al*, 2007), HMGB1 was decreased in the nucleus of Purkinje cells of Atxn1-KI mice (Fig 1A). In addition, HMGB1 was decreased in the cytoplasm of Purkinje cells (Fig 1A). In Atxn1-KI; HMGB1 mice, the expression of HMGB1 was restored to the level of background C57BL/6 mice in the nucleus and cytoplasm of Purkinje cells at 9 weeks (Fig 1A). The ubiquitin-positive aggregation of mutant Atxn1 was not largely affected by expression of exogenous HMGB1 when assessed by immunohistochemistry and Western blot analysis (Fig 1B and C), even though HMGB1 is a binding partner of mutant Atxn1 (Qi *et al*, 2007), probably because exogenous expression of HMGB1 was far smaller than endogenous expression (Supplementary Fig S1C). Meanwhile, immunostaining showed recovery of HMGB1 in the Purkinje cells of Atxn1-KI;HMGB1 mice (Fig 1A and B), reflecting an increase in Atxn1-unbound HMGB1 reactive to antibody.

Despite continued aggregation of mutant Atxn1, the Atxn1-KI; HMGB1 mice showed a remarkable improvement of motor activity in the rotarod test (Fig 1D and E). The improvement was obvious in comparison of multiple genotypes including Ku70-Tg mice and Atxn1-KI;Ku70 double-transgenic mice (Supplementary Fig S1H). Transgenic co-expression of Ku70 was effective for a Huntington's disease (HD) mouse model (R6/2 mice) (Enokido *et al*, 2010) but not effective for Atxn1-KI (Supplementary Fig S1H).

Moreover, the lifespan was extended dramatically (Fig 1F). The 50% and maximum survival durations were elongated from 217 days (Atxn1-KI) to 282 days (Atxn1-KI;HMGB1) and from 274 days (Atxn1-KI) to 360 days (Atxn1-KI;HMGB1), respectively. This elongation rate is one of the best results reported with Atxn1-KI mice (Watase *et al*, 2007). In our analysis, the thickness of the molecular layer was decreased at the onset of symptoms (9 weeks). Consistent with the improved motor activity, pathological examination revealed recovery of the molecular layer thickness in Atxn1-KI; HMGB1 mice at 9 weeks (Fig 1G and H).

HMGB1 expression restores nuclear DNA damage *in vivo*

Given that HMGB1 promotes DNA damage repair via architectural changes in genomic DNA (Bianchi & Beltrame, 1998; Agresti & Bianchi, 2003; Travers, 2003), we evaluated double-strand breaks (DSB) in genomic DNA by immunostaining and Western blot of phosphorylated

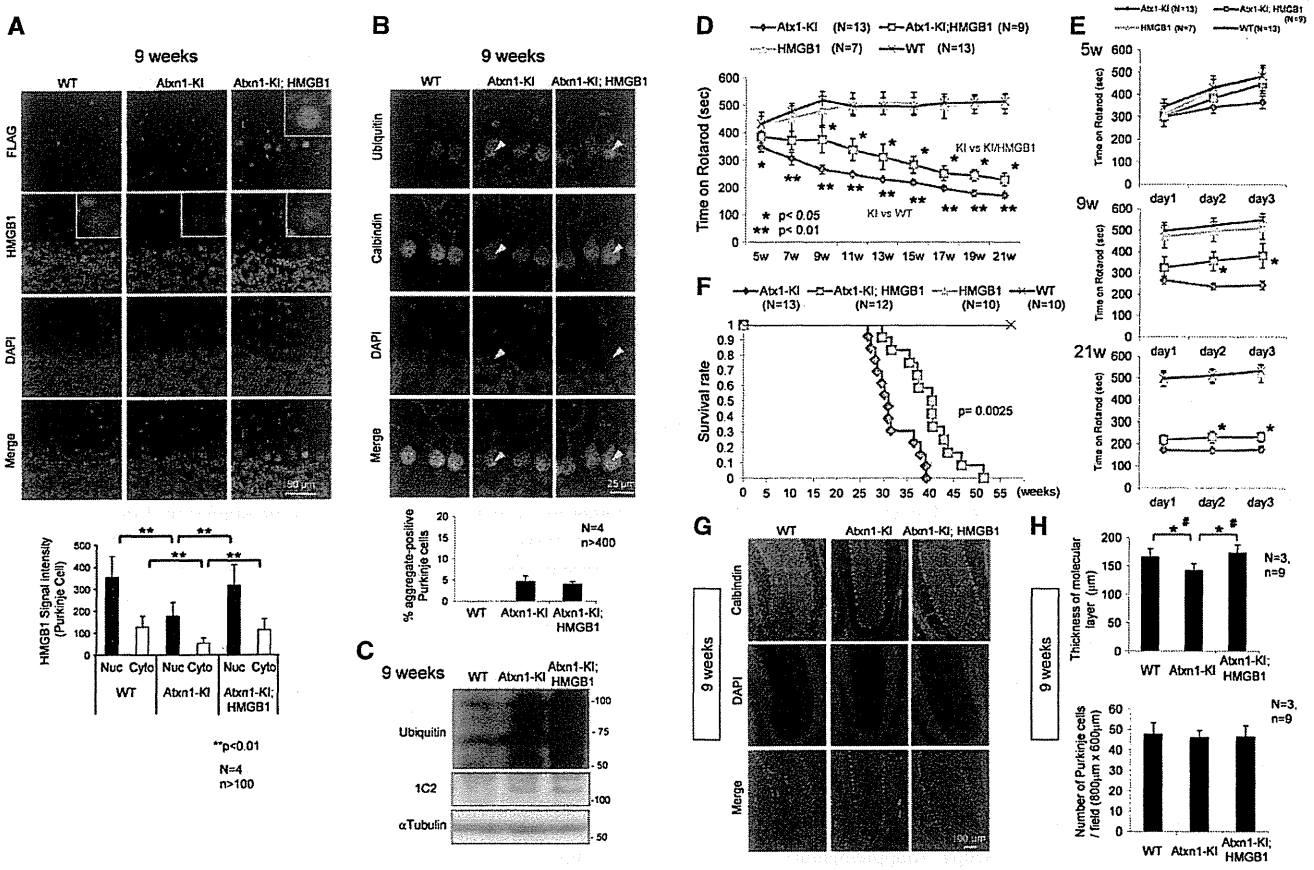

Figure 1. Symptomatic rescue of double-transgenic mice without decreased protein aggregation.

A The expression of exogenous HMGB1-FLAG (detected with an anti-FLAG antibody) and endogenous+exogenous HMGB1 (detected with an anti-HMGB1 antibody) was tested by immunohistochemical analysis. Nuclear and cytoplasmic signals were reduced in Atxn1-KI mice but restored in double-transgenic mice. The mean ± SD are shown in the lower graph.

B Aggregate formation was tested by immunohistochemical analysis of cerebellar tissues of background C57BL/6 mice, mutant Atxn1-KI mice and double-transgenic mice. Ubiquitin-positive aggregates were observed in mutant Atxn1-KI mice and double-transgenic mice (upper panels); the ratio of aggregate-positive Purkinje cells did not differ between the four mutant Atxn1-KI mice and the four double-transgenic mice (lower graph). The data are presented as mean ± SD.

C Western blot analysis with anti-ubiquitin antibody confirmed that aggregate formation was similar in mutant Atxn1-KI mice and double-transgenic mice.

D The rotarod performance test revealed improvement in the motor activity of double-transgenic mice over that of mutant Atxn1-KI mice. The time on rotarod was the mean value of the times from day 1 to day 3. The symptomatic onset in mutant Atxn1-KI mice was 7 weeks; improvement in double-transgenic mice lasted from 9 to 21 weeks. The data are presented as mean ± SD. Statistical analysis was performed with the Bonferroni–Dunn test and Student's *t*-test.

E Details of the rotarod performance of the three genotypes of mice (WT, Atxn1-KI and double-transgenic) from day 1 to day 3 at 5, 9 and 21 weeks. The data are presented as mean ± SD.

F The survival rates of the four genotypes of mice. The mean and maximum lifespans of double-transgenic mice were nearly 30% longer than those of mutant Atxn1-KI mice. The 50% survival duration was extended from 217 days (Atxn1-KI) to 282 days (Atxn1-KI;HMGB1), and the maximum survival duration was extended from 274 days (Atxn1-KI) to 360 days (Atxn1-KI;HMGB1). The effect of HMGB1 on the lifespan was assessed by Kaplan–Meier analysis, and the end-point postponement was significant in the log-rank test ($P = 0.0025$).

G Histological evaluation of the double-transgenic mice.

H Quantitative analysis of histological parameters in the three groups of mice showed that reduction in the molecular layer thickness was reversed in double-transgenic mice (upper graph; Student's *t*-test, $P < 0.05$). The mean thickness was quantified in more than 10 visual fields per mouse, and the mean ± SD was calculated for nine mice in each group. The number of Purkinje cells, similarly calculated, was not changed in mutant Atxn1-KI mice or in double-transgenic mice (lower graph). The data are presented as mean ± SD. $^{*}P < 0.05$ in Student's *t*-test, $^{\#}P < 0.05$ in one-way ANOVA followed by *post hoc* Tukey's HSD (honestly significant difference) test.

Source data are available online for this figure.

histone H2AX (γH2AX) or p53 binding protein 1 (53BP1) (Supplementary Fig S3). γH2AX signals were increased in Purkinje cells of mutant Atxn1-KI mice and recovered in those of Atxn1-KI;HMGB1 mice in immunohistochemistry (Supplementary Fig S3A), which was confirmed quantitatively (Supplementary Fig S3B). The results were reproduced by 53BP1 in both methods (Supplementary Fig S3A and C). Western blot analyses with γH2AX and 53BP1 antibodies also revealed the increase of DSB in Atxn1-KI mice and the recovery in Atxn1-KI; HMGB1 mice (Supplementary Fig S3D and E). Moreover, a negative relationship was observed between the γH2AX signal and HMGB1

signal in the Purkinje cells of Atxn1-KI mice (Supplementary Fig S3F and G). These results indicate that HMGB1 supplementation rescues DNA damage in Atxn1-KI mice, as expected from our previous results with primary neuronal cultures (Qi *et al*, 2007).

Mutant Atxn1 reduces mitochondrial HMGB1

HMGB1 is reported to exist in the cytoplasm and to regulate autophagy (Tang *et al*, 2010, 2011). Cytoplasmic HMGB1 binds to phosphorylated Beclin1 and deprives it from Bcl2. The HMGB1–Beclin1 complex accelerates autophagy and contributes to mitochondrial quality control (Tang *et al*, 2011). However, it is not yet clear exactly where in the cytoplasm HMG1 is located. Unexpectedly, our Western blot analysis with fractionated cellular compartments from mouse cerebellar tissues revealed mitochondrial HMGB1 in addition to the nuclear and cytosolic HMGB1 (Fig 2A). Moreover, HMGB1 in the mitochondria fraction was decreased in Atxn1-KI mice and recovered in Atxn1-KI;HMGB1 mice (Fig 2A). Consistently, overlapped signals between HMGB1 and Cox IV were decreased in Atxn1-KI mice in comparison with the background mice and restored in Atxn1-KI;HMGB1 mice (Supplementary Fig S4A).

To examine mitochondrial localization of HMGB1, we performed immunoelectron microscopy of cerebellar tissues from wild-type mice with anti-HMGB1 antibody. Silver staining, which enlarges gold particles by the complex, was used to enhance reaction (Fig 2B). As expected, we found gold particles in the matrix of mitochondria (Fig 2B, arrowhead). Peri-mitochondrial deposition of gold particles (Fig 2B, arrow) might be consistent with autophagy-related function of HMGB1. The three mouse genotypes were further examined by immunoelectron microscopy (Supplementary Fig S4B). Grain-positive mitochondria was decreased in Atxn1-KI mice but recovered in Atxn1-KI;HMGB1 mice (Supplementary Fig S4B). Immunostaining with normal IgG did not reveal grains in electron microscopy (Supplementary Fig S4C).

In order to confirm existence of HMGB1 in mitochondria, we purified mitochondrial fraction by Percoll density gradient centrifugation method (Sims & Anderson, 2008) and by isotonic homogenization method (Shimizu *et al*, 1998), in addition to mitochondrial preparation using commercial kit. In mitochondrial fractions prepared by both methods, we detected the band of HMGB1 by Western blot (Fig 2C). When mitochondrial fraction by Percoll density gradient centrifugation method was treated with proteinase K before membrane perforation, HMGB1 was not digested just like Cox IV, cytochrome c and TFAM, a transcription factor for mitochondrial genome that are localized at or inside of inner mitochondrial membrane (Fig 2D) (Parisi & Clayton, 1991). Tom20 at outer mitochondrial membrane was digested by proteinase K under the similar condition (Fig 2D), supporting the digestion was sufficient for proteins anchored or attached to the mitochondrial surface. After membrane perforation, all these mitochondrial proteins were completely degraded by proteinase K (Fig 2D). These results supported that HMGB1 exists inside of mitochondrial membrane.

HMGB1 may restore mitochondrial function through non-autophagic mechanism

As HMGB1 is implicated in autophagy (Tang *et al*, 2010, 2011), we performed electron-microscopic analyses expecting to detect changes of autophagy in Purkinje cells. However, we could not find any evidence to support an increase of autophagic vacuoles or of mitophagy in the cell bodies (Supplementary Fig S4D and E) and synapses (Supplementary Fig S4F) of Atxn1-KI mice although we found that the mitochondrial electron density was obviously decreased in Atxn1-KI mice (Supplementary Fig S4D). The interaction of HMGB1 and Beclin1, which was increased in the autophagy cellular model (Tang *et al*, 2010), was not also confirmed in our immunoprecipitation experiments with brain samples (Supplementary Fig S4G).

However, we found several findings to suggest functional impairment of mitochondria by mutant Atxn1. First, we found that mutant Atxn1 impaired mitochondrial dynamics. Mitochondrial fission and fusion were evaluated by live imaging (Jendrach *et al*, 2005) in HeLa cells (Supplementary Videos S1, S2 and S3). Compared with HeLa cells expressing DsRed (Supplementary Video S1), fission and fusion frequencies were decreased in HeLa cells expressing mutant Atxn1-DsRed (Supplementary Video S2), and the decrease was rescued by co-expression of HMGB1-EGFP (Supplementary Fig S3H, Supplementary Video S3). Second, analysis of membrane potential by MitoTracker Deep Red revealed reduced mitochondrial membrane potential in HeLa cells expressing mutant Atxn1 and the recovery by co-expression of HMGB1-GFP (Fig 3A). The change of mitochondrial membrane potential by HMGB1 was further tested with JC-1 (5,5′,6,6′-tetrachloro-1,1′,3,3′-tetraethylbenzimidazolylcarbocyanine iodide), a more direct indicator of in the mitochondrial membrane potential ($\Delta\Psi m$) and siRNA against HMGB1 (Fig 3B). As expected, transfection of two types of siRNAs changed the colour of JC-1 from red to green (Fig 3B) and suppressed HMGB1 protein (Fig 3C) in siRNA-transfected cells. Third, enzyme histochemistry revealed reduced activities of succinate dehydrogenase (SDH) and cytochrome c oxidase (CCO) activities in Purkinje cells of Atxn1-KI mice and their recovery in Atxn1-KI;HMGB1 mice (Fig 3D). Fourth, HMGB1 knock-down decreased TMRM (tetramethylrhodamine methyl ester) intensity in FACS analysis of HeLa cells by transiently expressing HMGB1-siRNA (Fig 3E).

These results collectively suggested that mutant Atxn1 damaged mitochondria via intrinsic mitochondrial function(s) related to HMGB1. Therefore, we next sought another hypothesis to explain the effect of mutant Atxn1 on mitochondria.

HMGB1 contributes to mitochondrial DNA quality control

From the localization of HMGB1 in the mitochondria matrix (Fig 2B) and deprivation of HMGB1 from mitochondria by mutant Atxn1 (Fig 2A and Supplementary Fig S4A and B), we speculated that HMGB1 might be relevant to the architectural control of mitochondria DNA. If this is the case, mitochondrial DNA damage repair should be affected. To address this question, we first investigated the ratio of long and short cDNA amplification from mitochondrial DNA, which is commonly used for the quantitative analysis of mitochondrial DNA damage (Das *et al*, 2010) based on the fact that nicks in mitochondrial DNA disturb cDNA extension. As expected, mitochondrial DNA damage in the cerebellar cortex was increased in Atxn1-KI mice, but not in Atxn1-KI;HMGB1 mice (Fig 4A). We also performed the chloramphenicol (CAP) resistance assay (Aamann *et al*, 2010) based on the fact that HeLa cells with mitochondrial

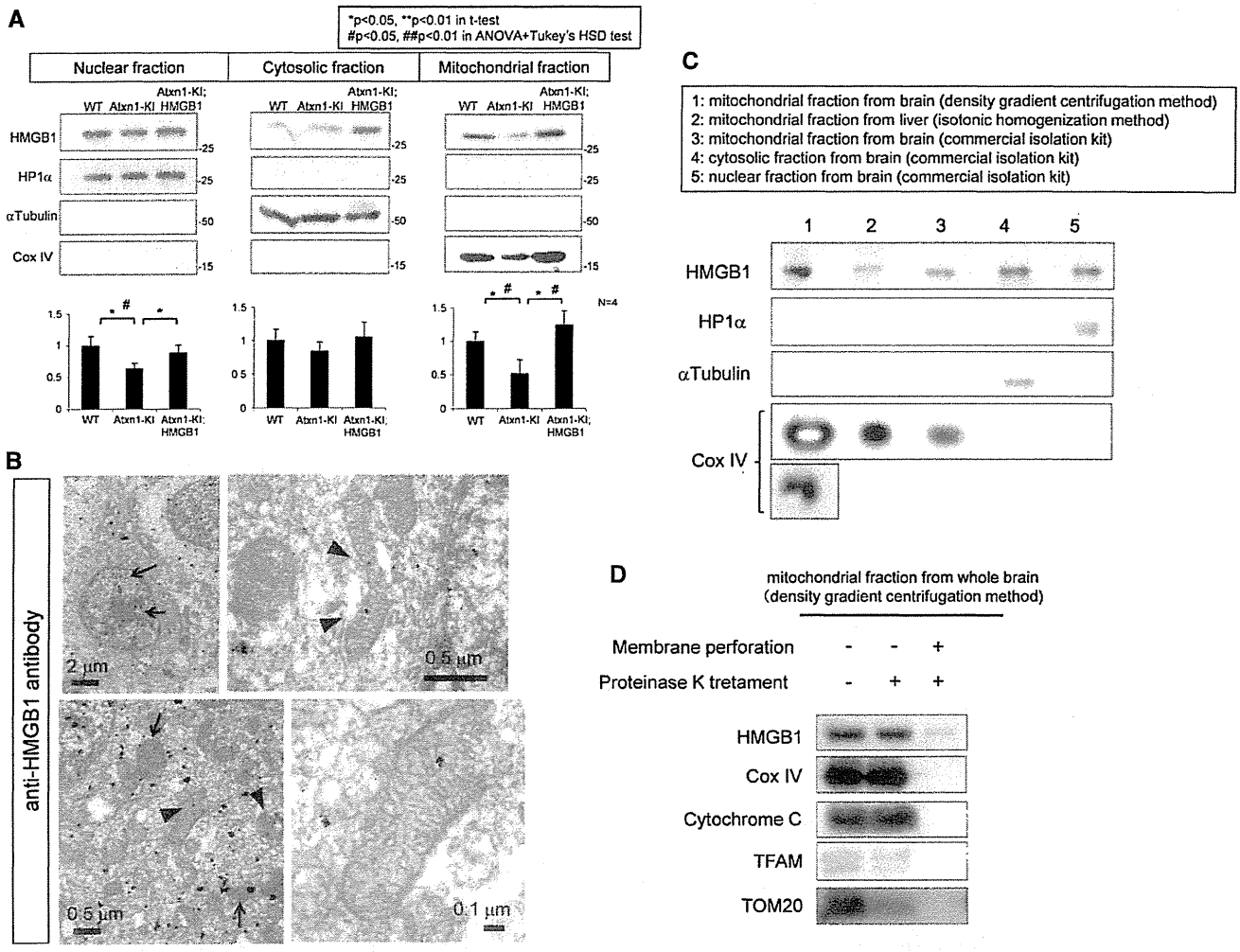

Figure 2. Mitochondrial HMGB1 is linked to mitochondrial functions.

A Western blot with separated cellular components from the cerebellar tissues of the three genotypes of mice showed that HMGB1 was decreased not only in the nucleus but also in the cytosol and mitochondria of mutant Atxn1-KI mice. The downregulation in the three subcellular fractions was reversed in the double-transgenic mice. The band intensity was quantified and is shown in the lower graphs. The data are presented as mean ± SD. Statistical analysis involved Student's *t*-test and one-way ANOVA followed by *post hoc* Tukey's HSD (honestly significant difference) test.

B Immunoelectron microscopy of the cerebellar cortex of control mice, with staining using an anti-HMGB1 antibody. Nucleus-dominant distribution of the gold–silver complex particles was found (arrows in the upper left panel), although the particles were also found in the cytoplasm. In the cytoplasm (lower left panel), the mitochondrial membrane (arrow) and matrix (arrowhead) were stained. Higher-magnification images of the mitochondrial matrix staining are shown in the upper and lower right panels.

C Western blot detection of HMGB1 in mitochondria purified by multiple methods. Lane 1: the mitochondrial fraction purified from the brain by the Percoll density gradient centrifugation method (Sims & Anderson, 2008), Lane 2: the mitochondrial fraction purified from the mouse liver by the other centrifugation method (Shimizu *et al*, 1998), Lane 3: mitochondrial fraction purified from the mouse brain using a commercial isolation kit), Lane 4: the cytosol fraction from the mouse brain isolated using the Mitochondria Isolation Kit (Thermo Scientific, IL, USA) and Lane 5: a nuclear fraction from the mouse brain isolated using the same kit. All the methods revealed the presence of HMGB1 in mitochondria.

D Proteinase K was added to the mitochondrial fraction prepared by the Percoll density gradient centrifugation method, to exclude the possibility of contamination with the nuclear or cytosolic fraction. Addition of proteinase K before membrane perforation did not affect HMGB1 dramatically decreased HMGB1 after membrane perforation, indicating that HMGB1 is located in the mitochondria. Other mitochondrial proteins including Cox IV and cytochrome c at the inner mitochondrial membrane or TFAM that binds to mitochondrial DNA inside the inner mitochondrial membrane showed a similar pattern of changes, whereas Tom20 at the outer mitochondrial membrane was digested before membrane perforation.

Source data are available online for this figure.

DNA damage become resistant to CAP. Again, the number of chloramphenicol-resistant colonies that possessed mitochondrial DNA damage was increased in HeLa cells expressing mutant Atxn1, but the increase was rescued by co-expression of HMGB1 (Fig 4B). Expression levels of mutant Atxn1 and HMGB1 were equal in Western blot analysis (Fig 4C).

Published online: December 15, 2014
EMBO Molecular Medicine

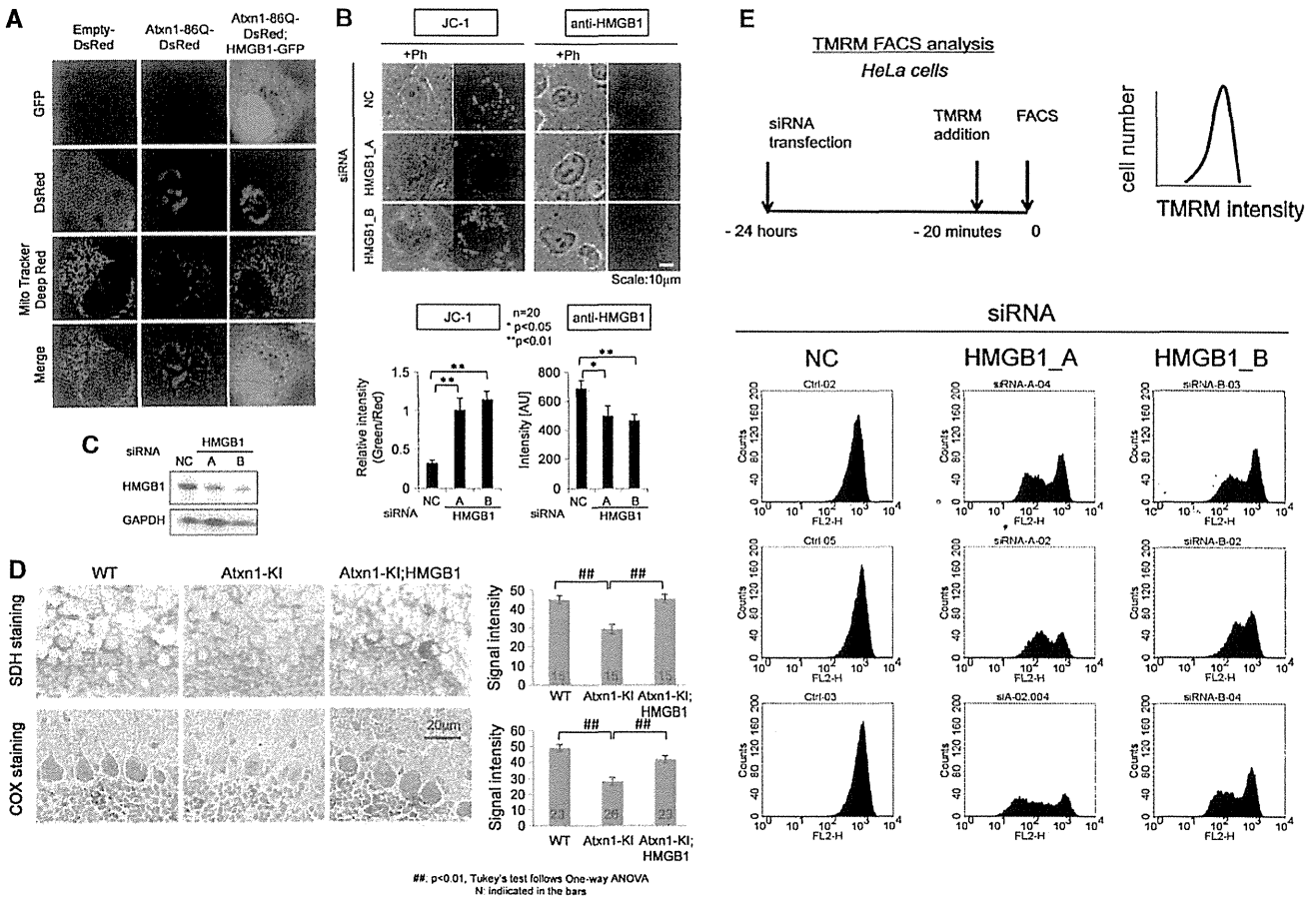

Figure 3. HMGB1 restores mitochondrial functions.

A The accumulation of MitoTracker Deep Red, a far red-fluorescent dye indicator of the mitochondrial membrane potential, in the mitochondria of mutant Atxn1(86Q)-DsRed-transfected HeLa cells was reduced by co-expression of HMGB1-GFP.

B A knock-down of HMGB1 by two types of HMGB1-siRNA (HMGB1_A, HMGB1_B) decreased the number of mitochondria with the normal membrane potential (stained red with JC-1) and increased the number of mitochondria with an abnormal membrane potential (stained green with JC-1). NC: negative control siRNA. Right panels show HMGB1 signals in the transfected cells.

C Expression levels of HMGB1 in the transfected cells used in (B) were confirmed by Western blot analysis.

D Mitochondrial enzyme histochemical analysis revealed reduction of succinate dehydrogenase (SDH) and cytochrome oxidase (COX) activity in Purkinje cells of Atxn1-KI mice. The reduced activity of these enzymes was restored in Atxn1-KI;HMGB1 mice.

E FACS analysis with the well-characterized potentiometric fluorescent dye tetramethylrhodamine methyl ester (TMRM) to quantify the changes of the mitochondrial membrane potential and mitochondrial permeability transition induced by HMGB1. The upper left panel shows experimental procedure, and the upper right panel shows parameters in the following graphs. Non-specific negative control siRNA did not affect TMRM signals, whereas siRNA-A and siRNA-B against HMGB1 substantially reduced a part of transfected HeLa cells. The siRNAs that were used for this analysis were similar to those in Supplementary Fig S8, where suppression of HMGB1 by these siRNAs was confirmed. The results from three sets of independent transfection experiments indicated that the mitochondrial membrane potential and mitochondrial permeability transition were changed by the deficiency in HMGB1.

Source data are available online for this figure.

Next, we evaluated mitochondrial DNA damage by direct sequencing of mitochondrial DNA (Fig 4D). The assay was based on the fact that length of read becomes shorter when the template DNA has a nick or a single-/double-strand break. We first separated mitochondrial fraction from cerebellar tissues of WT mice (background C57BL/6 mice), Atxn1-KI mice and Atxn1-KI;HMGB1 mice and extracted DNA. Using the samples as template, we performed direct DNA sequencing using next-generation sequencer (NGS). Each sample produced 5,000–6,000 reads. The read sequences were referenced to mitochondrial genome sequence database, and only the reads that matched to the mitochondrial genome sequence were selected for further analysis, and the reads matched to nuclear genome were excluded from the next analysis. We made histograms from the results of read frequency and read length in three genotypes of mice. The distribution of read length was shifted to the shorter range in Atxn1-KI mice, while the shift was recovered in Atxn1-KI;HMGB1 mice (Fig 4D). The shift and recovery was statistically confirmed using Friedman test with *post hoc* Wilcoxon rank-sum test. The difference was definite even with additional Bonferroni correction. Finally, NGS analysis revealed various types

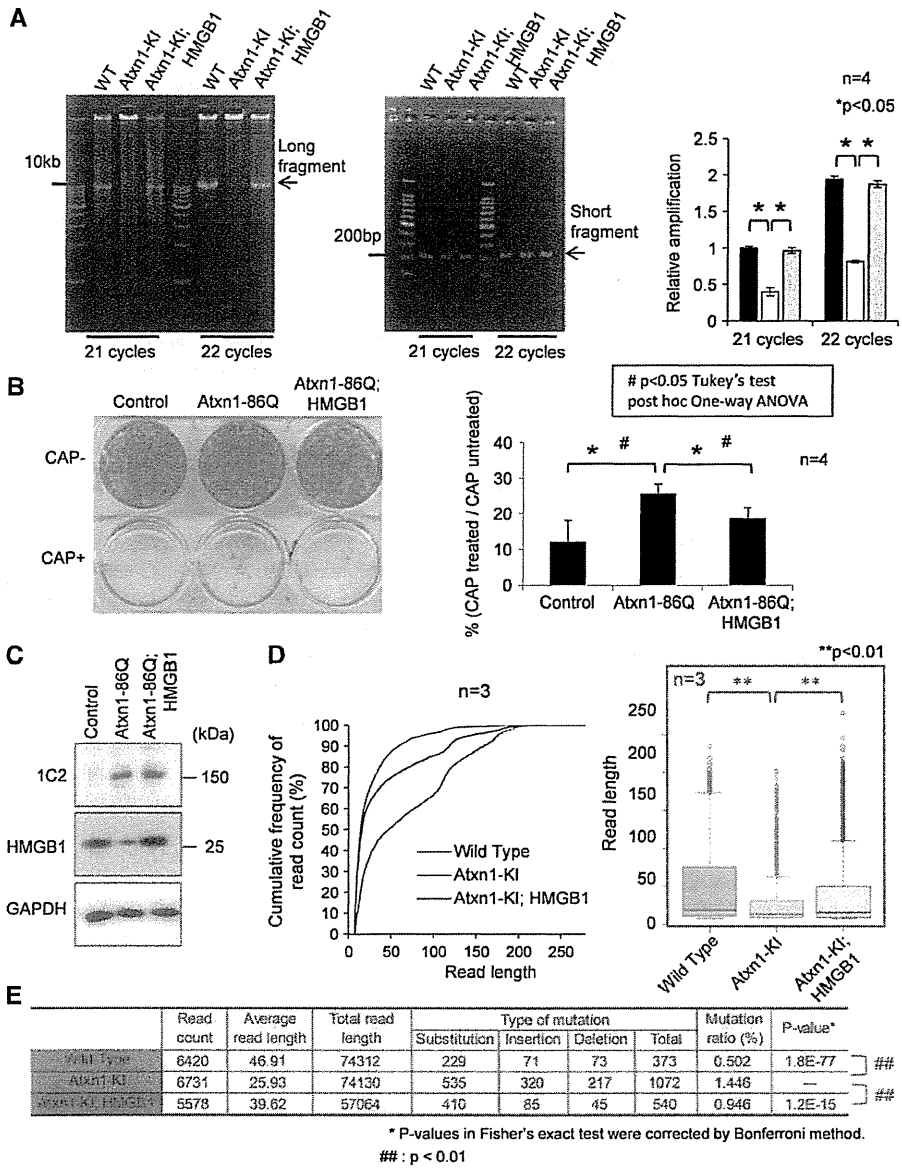

E

	Read count	Average read length	Total read length	Type of mutation				Mutation ratio (%)	P-value*	
				Substitution	Insertion	Deletion	Total			
Wild Type	6420	46.91	74312	229	71	73	373	0.502	1.8E-77	##
Atxn1-KI	6731	25.93	74130	535	320	217	1072	1.446	—	##
Atxn1-KI;HMGB1	5578	39.62	57064	410	85	45	540	0.946	1.2E-15	

* P-values in Fisher's exact test were corrected by Bonferroni method.
: p < 0.01

Figure 4. HMGB1 reverses mitochondrial DNA damage caused by mutant Atxn1.

A The mitochondrial DNA amplification assay with cerebellar tissue revealed that mitochondrial DNA damage was enhanced in mutant Atxn1-KI mice but reversed in the double-transgenic mice. The number of long cDNA fragments decreases when multiple DNA breaks occur between the primers, while short fragments are more easily amplified. The ratio of the long fragment to the short fragment was decreased in mutant Atxn1-KI mice (right panel). The data are presented as mean ± SD. Statistical analysis involved Student's *t*-test.

B The chloramphenicol (CAP) resistance assay of HeLa cells transfected with a control vector (pDsRed), Atxn1-86Q expression vector (pDsRed-Atxn1-86Q) or Atxn1-86Q expression vector + HMGB1 expression vector (pCI-HMGB1). The results showed an increase in mitochondrial DNA damage in mutant Atxn1-expressing HeLa cells. The increase was abrogated by co-expression of HMGB1. The data are presented as mean ± SD. Statistical analysis involved Student's *t*-test; $*P < 0.05$.

C Expression levels of Atxn1 and HMGB1 in transiently transfected HeLa cells used for the CAP assay in (B). Atxn1-86Q was detected with an anti-1C2 antibody.

D Analysis of mitochondrial genomic DNA using a next-generation sequencer. The cumulative percentages of read counts are plotted against the read length (left panel). The read lengths in the mitochondrial genome are also presented with box plots (right panel). Both analyses indicate that the read length was disproportionally shifted to the shorter fraction in Atxn1-KI mice. The shortening of the read length was reversed in Atxn1-KI;HMGB1 mice. The shift of distribution was analysed statistically using Friedman's test ($P = 2.19 \times 10^{-31}$) followed by Wilcoxon rank-sum test. *P*-values were corrected using the Bonferroni method. The *P*-value was 3.24×10^{-7} in the comparison between Atxn1-KI mice and background mice (wild-type) and 1.84×10^{-3} between Atxn1-KI;HMGB1 mice and Atxn1-KI mice.

E Frequency of mutation in the mitochondrial genome of the three genotypes of mice. The changes of mutation frequency were assessed statistically by Fisher's exact test and the *post hoc* Bonferroni correction. Mutation frequency was increased in Atxn1-KI mice compared to background mice (wild-type; $P = 3.24 \times 10^{-7}$) but normalized in Atxn1-KI;HMGB1 mice compared to Atxn1-KI mice ($P = 1.84 \times 10^{-3}$).

Source data are available online for this figure.

of mutations were actually increased in mitochondrial genome of the cerebellar tissues from Atxn1-KI mice, and they were recovered in Atxn1-KI;HMGB1 mice (Fig 4E). These results directly indicated that mitochondrial DNA damage was increased in the cerebellum of Atxn1-KI mice *in vivo*, and it was rescued by transgenic co-expression of HMGB1.

To evaluate the DNA damage repair activity in control, mutant Atxn1-expressing and mutant Atxn1/HMGB1-co-expressing L929 cells, the ratio of long and short cDNA amplification from mitochondrial DNA by PCR was calculated before and after X-ray irradiation (8 Gy) (Fig 5A) according to the reported method (Zhou *et al*, 2012). At 10 min after X-ray irradiation, DNA damage still remained in three types of cells (Fig 5B). From 10 to 180 min after X-ray irradiation, amplification of long fragment was improved in control cells and mutant Atxn1/HMGB1-co-expressing cells but not in mutant Atxn1-expressing cells (Fig 5B). Subtraction of the 10-min values from the 180-min values (Fig 5C) made the difference among three types of cells obvious in the recovery of mitochondrial DNA damage. HMGB1 clearly promoted the recovery from mitochondrial DNA damage (Fig 5C). The extents of DNA damage induced by X-ray irradiation at the initial time point were similar in three types of cells (Fig 5D), judging from quantification of 8-hydroxydeoxyguanosine (8-OHdG). In addition, expression levels of mutant Atxn1 were similar in mutant Atxn1-expressing cells and mutant Atxn1/HMGB1-co-expressing cells (Fig 5E). HMGB1 was increased in mitochondrial fraction of Atxn1/HMGB1 co-expressing cells (Fig 5E) without contamination of nuclear or cytosol fractions (Fig 5F).

The essential role of HMGB1 in mitochondrial DNA damage repair was further tested by siRNA-mediated knock-down experiments. In the CAP resistance assay performed in parallel with JC-1 experiment (Fig 3B) using the same siRNAs against HMGB1 (Supplementary Fig S4I), deficiency of HMGB1 (Supplementary Fig S4K) led directly to an increase in mitochondrial DNA damage. Consistently, shRNA-mediated knock-down of HMGB1 reduced the frequency of mitochondrial fission/fusion in HeLa cells (Supplementary Fig S4J). Together, these data support that HMGB1 contributes to mitochondrial DNA quality control and homeostasis.

HMGB1 directly interacts with and repairs damaged mitochondria DNA

To test direct involvement of HMGB1 in mitochondrial DNA repair, we performed several lines of experiments. First, we performed ChIP analysis with anti-HMGB1 antibody for mitochondrial DNA (Fig 6A). A DNA fragment of 1,849 bp was amplified with mitochondria-specific primers from purified mitochondrial fraction of HeLa cells expressing DsRed, Atxn1-33Q-DsRed or Atxn1-86Q-DsRed. The specific band amplified from mitochondrial DNA co-precipitated with HMGB1 was obviously increased after irradiation (Fig 6A, middle panel). Interestingly, the band was decreased in the presence of Atxn1 especially by mutant form expression. Expression levels of Atxn1-33Q-DsRed or Atxn1-86Q-DsRed were almost equivalent (Fig 6B).

Second, to evaluate the amount of mitochondrial DNA repair, we quantified incorporation of radioactive nucleotide into DNA in mitochondrial fraction of HeLa cells after X-ray irradiation (8 Gy) (Fig 6C). Damaged mitochondria was pretreated with anti-HMGB1 antibody or added with recombinant HMGB1 protein to test the effect of endogenous and exogenous HMGB1 protein on mitochondrial DNA damage repair. As expected, anti-HMGB1 antibody but not normal IgG inhibited mitochondrial DNA damage repair. HMGB1 recombinant protein recovered the inhibition by the antibody, and it also substantially enhanced mitochondrial DNA repair in the absence of anti-HMGB1 antibody (Fig 6C). All these results indicated that HMGB1 protein directly interacts with and promotes repair of mitochondrial DNA.

HMGB1 contributes to mitochondrial DNA repair *in vivo*

To confirm that HMGB1 actually contributes to repair of mitochondrial DNA damage *in vivo*, we analysed reversal of mitochondrial DNA damage in three genotypes of mice subjected to X-ray irradiation (20 Gy) under anaesthesia. Simultaneously, we compared the extent of impairment in the DNA damage repair function between the mitochondria and nucleus. Mitochondrial and nuclear DNA amplification assays were performed in parallel using the cerebellar tissue obtained from wild-type, Atxn1-KI and Atxn1-KI;HMGB1 mice before irradiation and 10, 180 and 300 min after irradiation (Fig 7A and B). Quantitative analysis of the ratio of long/short PCR fragments reconfirmed the increased DNA damage in both mitochondrial and nuclear genomes (Fig 7C and D). The recovery of the long/short PCR fragments ratio was remarkably retarded in both mitochondrial and nuclear genomes in Atxn1-KI mice from 10 to 300 min (Fig 7C and D). Subtraction of the ratio value at 10 min from that at 180 or 300 min further supported the delay of recovery in Atxn1-KI mice and the normalization in Atxn1-KI;HMGB1 mice (Fig 7E and F). A minor difference was that the rescue of DNA damage repair was significant in mitochondria but not in the nucleus from 10 to 180 min (Fig 7E and F).

Moreover, Southern blot analysis of mitochondrial genome DNA confirmed the difference in DNA damage in the default state of wild-type, Atxn1-KI and Atxn1-KI;HMGB1 mice at 13 weeks of age. Mitochondrial DNA copy numbers were largely similar across genotypes, while mitochondrial DNA was damaged substantially in Atxn1-KI mice, but not in Atxn1-KI;HMGB1 mice (Fig 7G). Quantification of signal intensity of the 16-kb band corresponding to the intact mitochondrial genome and of the DNA smear (1–16 kb) by ImageQuant LAS500 confirmed the difference among three genotypes of mice (Fig 7H).

HMGB1 supplementation improves gene expression profiles

Although the direct role of HMGB1 in mitochondrial DNA damage repair was strongly suggested, the indirect role through transcriptional regulation might be possible. Therefore, we decided to investigate changes of gene expression profile by mutant Atxn1 and HMGB1. First, Purkinje cells were purely isolated from frozen tissue sections using laser dissection (Supplementary Fig S5A). RNA was extracted from dissected Purkinje cells, amplified by PCR and submitted to microarray analysis. The gene expression profiles in wild-type, Atxn1-KI and Atxn1-KI;HMGB1 mice ($N = 3$ for each mouse model) revealed that 2.8% of the genes were significantly decreased and 3.1% of genes were significantly increased in Atxn1-KI mice in comparison with background C57BL/6 mice (Supplementary Fig S5B). Among the decreased and increased genes, 18.2 and 24.3% of the genes, respectively,

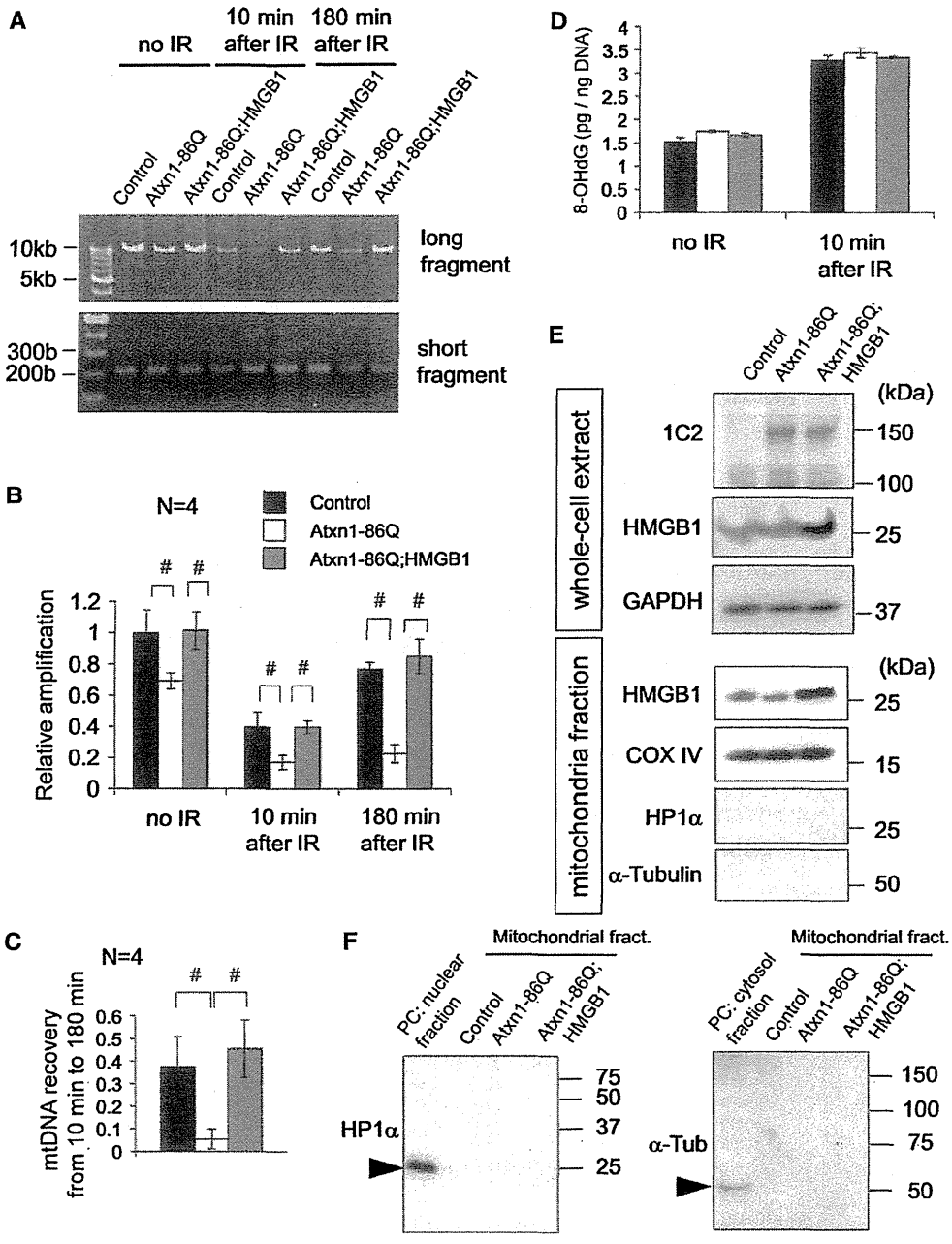

Figure 5. HMGB1 restores mitochondrial DNA repair after irradiation.

A The mitochondrial DNA amplification assay with L929 cells at two time points (10 and 180 min) after X-ray irradiation to induce DNA damage. Amplification of the long and short fragments from the mitochondrial genome was performed at each time point after irradiation in mock-transfected, Atxn1-86Q-expressing and Atxn1-86Q-HMGB1-coexpressing L929 cells that had been transfected 48 h before irradiation. The control cells were transfected with the same amount of empty plasmids.

B Quantitative analysis of DNA damage at each time point using the ratio between short and long PCR fragments (long/short). Reduction of the ratio indicates enhanced DNA damage. At any time point, DNA damage was induced by mutant Atxn1 and attenuated by HMGB1. The data are presented as mean ± SD. $^{\#}P < 0.05$ in one-way ANOVA followed by *post hoc* Tukey's HSD test.

C Reversal of DNA damage between minutes 10 and 180 was evaluated by subtraction of the values. Recovery was very small in Atxn1-expressing cells, but it was normalized by co-expression of HMGB1. The data are presented as mean ± SD. $^{\#}P < 0.05$ in one-way ANOVA followed by *post hoc* Tukey's HSD test.

D The extent of DNA damage evaluated using 8-OHdG was equivalent among the three types of transfection.

E Increased levels of mutant Atxn1 and HMGB1 after transfection were tested in whole-cell extracts and in the mitochondrial fraction. Mutant Atxn1 was equally expressed after two types of transfection, and HMGB1 was upregulated in cells and mitochondria.

F To verify the results from the mitochondrial fraction, blots with anti-HP1α and α-tubulin antibodies were performed with a positive control.

Source data are available online for this figure.